PPPL-2101

PPPL-2101

PPPL-2101
DE84 013098

LOWER HYBRID WAVE RESONANCE CONE DETECTION VIA CO_2 LASER SCATTERING

By

G.A. Wurden, K.L. Wong, and M. Ono

APRIL 1984

PLASMA PHYSICS LABORATORY

PRINCETON UNIVERSITY
PRINCETON, NEW JERSEY

PREPARED FOR THE U.S. DEPARTMENT OF ENERGY,
UNDER CONTRACT DE-AC02-76-CHO-3073.

LOWER HYBRID WAVE RESONANCE CONE DETECTION VIA CO_2 LASER SCATTERING

G. A. Wurden*, K. L. Wong, and M. Ono

Plasma Physics Laboratory, Princeton University
Princeton, NJ 08544

ABSTRACT

Lower hybrid waves are studied in the Princeton ACT-I steady-state toroidal plasma device using a radially scanning CO_2 laser scattering system with both amplitude and phase sensitive detection techniques. Clearly defined resonance cones launched from external electrostatic antennas are seen to disappear as the plasma density is raised. Scaling of LHW laser signal with RF power in the presence of resonance cones, shows nonlinearities associated with RF induced changes in the effective laser scattering volume. Absolute fluctuation level estimates suggest this occurs when $e\Phi/T_e \geq 1$. Wavefront curvature effects can cause a complete loss of resonance cone laser signals, even though probes indicate that cones are still present. Measurements of the wave $k_\perp$-spectrum in the plasma show direct evidence for electron Landau filtering of the original wave $k_\parallel$-spectrum launched from the antenna at the plasma edge, and strong dependence on antenna phasing. Finally, frequency shifts and loss of the resonance cone signal are associated with high levels of plasma density edge turbulence.

I. INTRODUCTION

The detection of lower hybrid waves (LHW) by nonperturbing means has become more important recently due to promising heating and current drive applications of high power LHW in large tokamaks.[1,2] The technique of electromagnetic wave (CO_2 laser) scattering was first applied by Surko and Slusher[3] to driven lower hybrid waves in the ATC tokamak in 1976, but no signal was seen down to a density fluctuation level $\tilde{n}/n \sim 10^{-3}$. Microwave scattering was successfully used on the Princeton H-1 linear device in 1978,[4] but no radial or angle scanning capability was available. It was not until 1979 that driven LHW were observed at the level $\tilde{n}/n \sim 10^{-4}$ by CO_2 laser scattering on Alcator A , but resonance cones were not detected, and spectra of the LHW laser signal indicated probable heavy scattering by low frequency turbulence.[5,6] Lower hybrid waves have also been observed by coherent scattering of 2-mm microwaves in the WEGA stellerator/tokamak,[7] further suggesting that in this case, the LHW are not localized in resonance cones.

To address issues not easily answered in large experiments, we utilize a small steady-state toroidal plasma in conjunction with CO_2 laser scattering and electrostatic probes to make measurements on LHW launched from antennas at the edge of, or in the plasma itself. A high frequency lock-in technique is used for signal enhancement, allowing low-level detection while retaining phase information, facilitating comparison with probe measurements. We take advantage of the steady-state Advanced Concepts Torus (ACT-I),[8] by scanning the laser system continuously across the outer radius of the plasma, while also having the ability to sweep the laser scattering angle, corresponding to scattered wavenumbers $k_\perp^o \simeq 25$ to $120\ cm^{-1}$. The lower hybrid wave $k_\parallel$-spectrum can therefore be inferred by the laser, but not readily from probes. Such information is vital to quantitative understanding of LHW excitation and damping.

This paper reports studies of lower hybrid waves in the frequency range of 30 - 190 MHz in the ACT-I hydrogen plasma, using CO_2 laser scattering and probes to detect, respectively, the wave density fluctuation $\tilde{n}$ and wave electric potential Φ. Lower hybrid waves are excited by electrostatic plate-antenna arrays located on the midplane outer edge of the plasma (in the limiter shadow), and detected toroidally 15 cm to 340 cm away from the launcher. Most measurements are concentrated in the regime $1 < \omega/\omega_{pi} \leq 3$, close to the lower hybrid layer at which $\omega/\omega_{\ell h} = 1$, where $\omega_{\ell h} \equiv \omega_{pi}(1 + \omega_{pe}^2/\omega_{ce}^2)^{-1/2}$. Here ω_{pi},

ω_{pe}, and ω_{ce} have the usual definitions of ion plasma, electron plasma, and electron cyclotron frequency, respectively.

Resonance cones are detected with the laser system, and wave $k_{\parallel}$-spectra are measured both by scanning the scattering k-vector ($k_{\perp}^{o}$) with fixed plasma conditions, and by sweeping the density while holding $k_{\perp}^{o}$ constant. In this manner, the effects of antenna phasing and electron Landau damping on the LHW $k_{\parallel}$-spectrum in the plasma are observed. Extensive two-dimensional plasma parameter profiling shows the importance of planar wave-fronts to aid detection of the low (absolute) level RF waves with laser scattering. Power scaling shows nonlinear effects associated with background neutral ionization, and subsequent buckling of plasma profiles. Finally, high levels of low-frequency turbulence are seen to destroy the laser resonance cone signal.

In Sec. II, a brief theoretical background relevant to the experimental measurements is presented, and in Sec. III the experiment is described. Results of the experiment are presented in Sec. IV, with a discussion of the data and summary in Sec. V.

II. THEORY

A. Basic scattering concepts

The theory of light scattering from plasmas is well-known, and has been applied for measuring a wide range of plasma parameters.[9] The particular application of CO_2 laser scattering to study density fluctuations in plasma has been pioneered by Surko and Slusher.[10-12]

We first establish some fundamental parameters of interest. For the laser wavelength λ_o = 10.6 μm, all plasma waves under consideration will have $\lambda_{\perp} >> \lambda_o$ so that scattered light satisfying the Bragg condition

$$\theta_B = 2 \sin^{-1}\left(\frac{\lambda_o}{2\lambda_{\perp}}\right) , \qquad (1)$$

will always be at small angles (θ = 3-20 mrad for $\lambda_{\perp}$ = 3 - 0.5 mm) to the incident laser beam. From Gaussian optics, a freely expanding Gaussian beam has a diffraction limited half-angle $\Delta\theta = \lambda_o/\pi a_o$, where a_o is the beam waist, defined as the radius where the beam electric field amplitude has fallen to 1/e

of its central value. Choosing a coordinate system with regard to the machine, we take the z axis along B, the x axis along the midplane radius, and the y axis is vertical. The incident Gaussian laser beam is assumed to be linearly polarized, as shown in Fig. 1, with the electric field vector lying in the scattering plane. E_o and E_s are the magnitudes of the incident and scattered electric fields.

In general, we would like k_y of the plasma wave to be zero, and the driven wave to be planar over the scattering region. In practice, these two assumptions are violated in various degrees, and must be treated carefully. The scattering length in the y direction (essentially along the beam) is defined to be L_y = min (L_v, L_A, plasma diameter) , where L_v is the length determined by when the magnitude of the cross beam electric field amplitude $|E_o E_s|$ has fallen to 1/e of its maximum value (see Fig. 1), and L_A is the antenna height. In ACT-I, we have $L_y \propto L_A$ in all cases. For a monochromatic plane wave density fluctuation with frequency $\omega_o/2\pi$, of the form $\tilde{n}_e = \hat{n} \cos(k_\perp x - \omega t)$, it can be shown that the laser power scattered into the coherent solid angle $d\Omega = \pi(\lambda_o/\pi a_o)^2$, when $k_\perp$ of the wave matches $k_\perp^o$ given by the Bragg angle, is

$$P_s = \frac{1}{4} r_o^2 \lambda_o^2 P_o (\hat{n} L_y)^2 \quad . \tag{2}$$

where r_o is the classical electron radius e^2/mc^2, P_s is the scattered power, and P_o is the incident laser power. In practice, the wave phase may vary from the top to bottom of the laser scattering volume, so that destructive interference occurs, reducing the scattering length to a value denoted by L_{eff}. The phase fronts may be tilted with respect to the direction defined by $k_\perp^o$, in which case $L_{eff} = L_y \sin(X)/X$, where $X \equiv k_\perp \theta_{tilt} L_y/2$. Furthermore, the phase fronts may have a net curvature, in which L_{eff} can be approximated by the distance over which a relative phase shift of $\pi/2$ occurs. The worst case analysis would be random phasing over the laser scattering volume, for which the scattered power is proportional to $\hat{n}L$. However if this occurs, no signal would be seen in our experiment, due to the low absolute density of the ACT-I plasma. We operate well into the limit of coherent scattering, that is to say that $\alpha \equiv 1/k_\perp \lambda_{De} > 1$. The laser signal corresponds to scattering off electron density fluctuations which may be correlated with ion motion, but not to scattering off the ions themselves, due to their small Thomson cross section.

B. Dispersion relation

The fluctuating electron density driven by lower hybrid waves can be derived from the full electromagnetic wave equation and the continuity equation for electrons.[13] For completeness, we present a multispecies warm ion approach, which can then be reduced to the cold ion approximation when appropriate.

We will consider electrostatic waves in a multispecies warm-ion, cold electron plasma, in the frequency regime $\omega \geq \omega_{lh} \approx \omega_{pi} >> \omega_{ci}$. Here ω_{cj} is the ion cyclotron frequency of the j^{th} ion species, and the lower hybrid frequency is given by $\omega_{lh}^2 = \sum_j \omega_{pj}^2 (1 + \omega_{pe}^2/\omega_{ce}^2)^{-1}$. Experimentally, we operate in the parameter ranges shown in Table 1. We will use a local approximation by assuming that gradient scale lengths are long compared to $\lambda_\perp$, ie., that the WKB approximation $k_\perp^{-2}(dk_\perp/dx) << 1$ can be satisfied (true for ACT-I except near turning points and resonances). The full electromagnetic wave equation for a Fourier component of the form $e^{i\vec{k}\cdot\vec{r} - i\omega t}$ is then $\vec{n} \times (\vec{n} \times \vec{E}) + \vec{K} \cdot \vec{E} = 0$, where $\vec{K}$ is the hot plasma dielectric tensor.[13] The geometry is chosen so that B_o is along z, and , with little variation in plasma parameters in the y direction, we take $k_y = 0$. More explicitly:

$$\begin{pmatrix} K_{xx} - n_\parallel^2 & K_{xy} & n_\perp n_\parallel + K_{xz} \\ -K_{xy} & K_{yy} - n^2 & K_{yz} \\ n_\perp n_\parallel + K_{xz} & -K_{yz} & K_{zz} - n_\perp^2 \end{pmatrix} \cdot \begin{pmatrix} E_x \\ E_y \\ E_z \end{pmatrix} = 0 , \tag{3}$$

where $n \equiv kc/\omega$, and $\parallel$, $\perp$ denote components parallel and perpendicular to the magnetic field, respectively. In a nondrifting Maxwellian plasma, with $T_\perp = T_\parallel$, using $k_\perp \rho_e << 1$, the dielectric tensor elements of importance can be written approximately as

$$K_{xx} = 1 + \frac{\omega_{pe}^2}{\omega_{ce}^2} + \sum_j \frac{\omega_{pj}^2}{\omega\, k_\parallel v_j} \frac{\exp(-b_j)}{b_j} \sum_{n=1}^{\infty} n^2 I_n \left(Z_n + Z_{-n} \right) ,$$

$$K_{xy} = -i\frac{\omega_{pe}^2}{\omega\,\omega_{ce}} + i\sum_j \frac{\omega_{pj}^2}{\omega\, k_\parallel v_j}\exp(-b_j)\sum_{n=1}^{\infty} n(I_n - I_n')(Z_n - Z_{-n}) , \qquad (4)$$

$$K_{yz} = -\frac{\omega_{pe}^2}{\omega\,\omega_{ce}}\left(\frac{v_e^2}{c^2}\right)\xi_{eo}^2\left[1 + \xi_{eo}Z_o\right] ,$$

$$K_{zz} = 1 + \frac{2\,\omega_{pe}^2}{\omega^2}\,\xi_{eo}^2\left[1 + \xi_{eo}Z_o\right] ,$$

where the summation over j refers to ion species, I_n is the modified Bessel function of argument $b_j \equiv k_\perp^2 T_j/m_j\omega_{cj}^2$, and Z_n is the plasma dispersion function[14] with argument $\xi_{\sigma n} \equiv (\omega + n\omega_{c\sigma})/k_\parallel v_\sigma$, where the index σ refers either to ions or electrons. We note here that $n_\perp n_\parallel \gg K_{xz}$ so we neglect K_{xz}, and further that $K_{yy} = K_{xx}$, so we replace K_{yy} with K_{xx}. In most cases of interest, K_{yz} can also be neglected. Setting the determinant of the 3×3 matrix to zero yields the dispersion relation $D(\vec{k},\omega) = 0$.

At this point, without further approximation, we have available a numerical code[15] which solves for $k_\perp$, given $k_\parallel$ and the plasma parameters as inputs, keeping up to 40 terms in the Bessel function series if necessary. Contributions to the damping rate from ions and electrons are included (Landau and cyclotron), while collisional damping is usually unimportant for ACT-I parameters. Inverse damping lengths are calculated from the usual Taylor series expansion of the dispersion relation about a root with $\vec{k} = \vec{k}_r + i\vec{k}_i$, where $|k_r| \gg |k_i|$, and $\vec{k}_i$ is given by

$$\vec{k}_i = \frac{-D_i(\vec{k}_r)}{\left.\dfrac{\partial D_r}{\partial \vec{k}_r}\right|_{\vec{k}_r}} . \qquad (5)$$

D has been split into real and imaginary parts. The contribution from linear electron Landau damping is appreciable for $\xi_e \leq 3$, and can be expressed as $k_\parallel^i = \sqrt{\pi}\, k_\parallel^r\, \xi_e^3 \exp(-\xi_e^2)$. A ray tracing trajectory is followed into the plasma, estimating the wave energy density and energy flow along the way, including both the nonelectromagnetic and Poynting fluxes.

For analytic purposes, away from regions of linear turning points (if present in the plasma), the cold ion, cold electron approximation yields the usual cold electrostatic lower hybrid dispersion relation in a multispecies plasma,

$$1 - \frac{\omega_{pe}^2}{\omega^2}\left(\frac{k_\parallel^2}{k^2}\right) - \sum_j \frac{\omega_{pj}^2}{\omega^2 - \Omega_j^2} = 0 \quad . \tag{6}$$

Furthermore, the lower hybrid waves are expected to propagate into the plasma following resonance cone trajectories,[16] where the local cone angle $\theta = k_\parallel/k_\perp$ is dependent only on the electron density if $\omega \gg \omega_{pi},\ \omega_{ci}$.

C. LHW density fluctuation

Consider the electron density fluctuation $\tilde{n}_e$ associated with a single wave Fourier component. For lower hybrid waves, it is actually possible to have $\tilde{n}_e = 0$ even though the wave electric fields are finite.[6,7] So, in contrast to the signal from a probe, the laser signal could be zero, even though the wave might be present. From the continuity equation for electrons, one obtains $\tilde{n}_e = n_e \vec{k}\cdot\vec{v}^e/\omega$, where $\vec{v}^e$ is the electron response to an oscillating field in the plasma

$$\vec{v}^e = i\,\frac{e\omega}{m\omega_{pe}^2}\,\overleftrightarrow{K}^e \cdot \vec{E} \quad . \tag{7}$$

The previously defined dielectric tensor has been split into the vacuum, ion, and electron terms $\overleftrightarrow{K} = \overleftrightarrow{I} + \overleftrightarrow{K}^i + \overleftrightarrow{K}^e$. Using the cold electron approximation, from Eq. (4), we have

$$\tilde{n}_e = i \frac{en_e}{m\omega^2} k_x E_x \left(\frac{\omega^2}{\omega_{ce}^2} - \frac{\omega}{\omega_{ce}} \frac{iE_y}{E_x} - \frac{k_z E_z}{k_x E_x} \right) \quad . \tag{8}$$

The first term in Eq. (8) can be identified with polarization drift in the x direction, the second with ExB drift, and the third with electron inertia along field lines. The ratios of electric fields are found from Eq. (3), setting K_{xz} and K_{yz} to zero. One then obtains the (complex) fluctuating electron density, which can be written in two equivalent forms:

$$\tilde{n}_e = i\, n_e \frac{e}{m\,\omega\,c}\, n_\perp E_x \left(\frac{\omega^2}{\omega_{ce}^2} - \frac{\omega}{\omega_{ci}} \frac{iK_{xy}}{(K_{xx} - n^2)} + \frac{n_\parallel^2}{(K_{zz} - n_\perp^2)} \right)$$

or, (9)

$$\tilde{n}_e = -i\, n_e \frac{e}{m\,\omega\,c}\, n_\parallel E_z \left(- \frac{\omega^2 (n_\perp^2 - K_{zz})}{\omega_{ce}^2 n_\parallel^2} + \frac{\omega (n_\perp^2 - K_{zz}) iK_{xy}}{\omega_{ce} n_\parallel^2 (K_{xx} - n^2)} + 1 \right) \quad .$$

A zero of $\tilde{n}_e$ in the LHW frequency range occurs for $\omega = \omega_{pi}(1+\delta)$, where δ is a small positive number, as a result of cancellation between the electron inertia and polarization drift terms, and is present in both the cold and hot-ion approximations. This can be seen by balancing the first and third terms in Eq. 9, while simultaneously satisfying the cold LHW dispersion relation, which can be done for $\omega = \omega_{pi}$. In the ACT-I parameter range, the K_{xy} term in Eq. (9) can be neglected, and for a cold LHW, a good approximation for $\tilde{n}_e$, is given by

$$\tilde{n}_e = -i \frac{k_\perp E_x}{4\pi e} \left(1 - \omega_{pi}^2/\omega^2 \right) \quad , \tag{10}$$

which reduces to the simple Poisson result if $\omega \gg \omega_{pi}$. For $\omega > \omega_{pi}$, finite ion temperature effects on $\tilde{n}_e$ enter primarily through $k_\perp$, and for lower hybrid waves are usually neglected.[2,6] However, finite ion temperature effects should be

included for $\omega_{lh} < \omega \leq \omega_{pi}$, due to the large modifications occurring in $k_\perp$. Warm ion effects tend to shift the zero in $\bar{n}_e$ to slightly lower densities (ie., sooner along a ray trajectory). If mode conversion of the lower hybrid wave to a hot plasma wave[17] is predicted for a particular wave $k_\parallel$-component before the zero is reached, then finite ion temperature effects actually cause the zero to appear at significantly lower densities than cold plasma theory indicates. For ACT-I parameters, $\bar{n}_e = 0$ at $\omega \simeq 1.1\ \omega_{pi}$. Code runs at fixed $\lambda_\parallel$ show this zero to occur in such a narrow density band for ACT-I, close to the LH resonance where field swelling is also occurring, as to be all but unobservable in an actual experimental situation.

Having related the wave density fluctuation to the wave electric field, it remains for us to obtain the associated wave power. The total energy flux crossing a surface perpendicular to the y-z plane, is the wave power per unit area

$$P_\perp \equiv (S + T)_\perp = W_o\, v_{g\perp} \quad , \tag{11}$$

where S is the Poynting flux and T is the nonelectromagnetic energy flux associated with coherent motion of the particles. W_o is the wave energy density[13] and $v_{g\perp}$ is the perpendicular component of the group velocity, $v_{g\perp} \equiv \partial\omega/\partial k_\perp$. For the lower hybrid wave, neglecting the electromagnetic field energy, and locally ignoring dissipation, we write

$$W_o = \frac{1}{16\pi}\, \vec{E}^* \cdot \frac{\partial}{\partial\omega}\, (\omega\, \vec{K}) \cdot \vec{E}$$

$$\simeq \frac{|E|^2}{16\pi}\, \omega\, \frac{\partial D}{\partial\omega} \quad , \tag{12}$$

having used the electrostatic form of the dispersion relation $D(\vec{K},\omega) = 0$. The group velocity can be eliminated in Eq. (11) to yield

$$P_\perp = \frac{\omega}{k_\perp}\left(k_\perp \frac{\partial D}{\partial k_\perp}\right)\frac{E_\perp^2}{16\pi} \quad . \tag{13}$$

having neglected E_z^2, compared to $E_\perp^2$. It follows from Eq. (6) for a cold lower hybrid wave, that although the field and particle energy density is evenly divided, the energy flux is carried by the fields, so that

$$P_\perp = \frac{E_\perp^2}{8\pi}\frac{\omega}{k_\perp}\left(1 - \omega_{pi}^2/\omega^2\right) \quad . \tag{14}$$

where $E_\perp$ is a peak electric field strength, and $P_\perp$ is the wave power per unit area perpendicular to B_o for a monochromatic wave. Relating the wave power to the density fluctuation via Eq. (10), we obtain

$$\tilde{n}^2 = P_\perp \frac{k_\perp^3}{2\pi e^2 \omega}\left(1 - \omega_{pi}^2/\omega^2\right) \quad . \tag{15}$$

This shows the lowest order correction as ω approaches ω_{pi} from above, and reduces to previous results[4,6] for $\omega >> \omega_{pi}$.

III. EXPERIMENTAL APPARATUS

A. Plasma

The experiments were conducted in the ACT-I multispecies hydrogen plasma, using a hot tungsten filament plasma source.[8] The resulting steady-state toroidal plasma can be characterized by $n_e \simeq 1\times10^{10}$ cm^{-3} to 2×10^{11} cm^{-3}, $1 \leq T_e \leq 4$–6 eV, $0.025 \leq T_i \leq 2$ eV, $B_o \simeq 4.5$ kG, $R = 59$ cm, $a \leq 9$ cm, and hydrogen ion concentrations $H_1^+ \simeq 50$–80 %, $H_3^+ \simeq 30$ %, with the remainder H_2^+.[18] A typical configuration showing diagnostic access, antenna locations, and machine geometry is shown in Fig. 2. Twenty-six chamber sections form the torus. Straight side limiters, located at $r = 6$ cm at the outer midplane radius, reduce the plasma shape to an inverse D. This was done to match plasma edge conditions

to the vertical plate antennas used to launch plane wave lower hybrid waves, as we shall see later. Electrostatic floating double probes for wave measurements at various toroidal locations, as well as biased probes for monitoring the ion saturation current, can be scanned across the outer half of the torus in an x-y fashion. Vertical field correction coils can be energized to correct for minor magnetic field errors, thereby enhancing the vertical symmetry of the plasma, as shown in Fig. 3. A relatively uniform ion saturation current profile is obtained in the y direction by adding radial and vertical field components of a few gauss, thereby affecting the drift of fast electrons from the tungsten filament in the inner half of the torus. Wave studies are made on the outer half of the torus, in the diffuse plasma region, free of fast electrons. Ion temperature was measured by laser scattering on ion Bernstein waves,[19] and scales roughly inversely with neutral fill pressure. The electron density is measured by the lower hybrid resonance cone technique.[18] Here a lower hybrid wave is launched from the edge of the plasma with frequency $\omega >> \omega_{pi}, \omega_{ci}$ to determine the local cone angle $\theta \approx k_{\parallel}/k_{\perp} = \Delta x/\Delta z$, found by measuring the relative radial displacement Δx of two LHW cones launched from antennas with known toroidal separation Δz. The electron plasma frequency is determined from Eq. (6). By using a range of frequencies, or shifting to adjacent sets of antennas (or probes), the entire profile over the outer half of the machine can be covered. This is the most accurate absolute local density measurement (better than 10%), which we then use to calibrate the density inferred from Langmuir probe ion saturation current profiles. For densities higher than $\sim 1\times10^{11}$ cm^{-3}, ACT-I is equipped with an 8-mm microwave interferometer, which gives line averaged central chord measurements.

Typical electron density and low-frequency fluctuation profiles are shown in Fig. 4. The electrostatic vertical plate antennas are located in the limiter shadow, at r = 6.5 cm for measurements in this paper. Low frequency fluctuations peak near the plasma edge in regions of steep gradients, and are found to play an important role, affecting the propagation of lower hybrid waves.[20,21]

B. RF antennas

A series of antennas are employed in conjunction with the laser scattering experiment. The simplest is a 1"×1" fine mesh, parallel to B_o, which can be swung into place in the plasma midplane, 2-5 cm toroidally from the laser

scattering window. This is called the "close internal grid." An RF voltage applied to the grid drives large density fluctuations, observable by the laser. It is useful for initial alignment or launching a harmonic ion Bernstein wave, which might otherwise be absorbed by intervening harmonic layers if launched from the plasma edge.

The second type of antenna is placed in the shadow of a limiter, and relies upon electrostatic excitation of an electron plasma wave in the low density edge plasma by RF applied to copper plate(s). These slow waves then propagate into the plasma, becoming either ion Bernstein or lower hybrid waves, depending upon the frequency regime. Lower hybrid waves are excited by phased arrays of copper plates (see Fig. 2), with usually only the inner four of the six plates being driven with RF. If the outer two plates are driven as well, then they tend to dominate over the inner ones, and phasing control is lost. Two LHW antenna designs have been used here. The first consisted of simple straight plates (Fig. 5a), with spacing 1.3 cm per plate, but these tended to excite high $n_{\parallel}$ components due to their δ-function-like nature. The second version consisted of "bent-plate" 6-element arrays, as shown in Fig. 5a, with the width of the bent piece one-half the 1.3 cm spacing. If phased by π, these should give a dominant $\lambda_{\parallel} \approx 2.6$ cm, or if phased by $\pi/2$, then $\lambda_{\parallel} \approx 5.2$ cm. In practice, it was found that feeding just the center plate gave a better laser signal, perhaps due to the broader $\lambda_{\parallel}$ spectrum launched. Finally, as seen in Fig. 5b, these antennas could be tilted as a whole while the machine is running. The tilt range is small (±30 mrad), but was found to play an important role in optimizing the alignment between the launched wave and the laser scattering vector orientation.

Supporting wave measurements were carried out using both single and double tip floating microcoaxial probes, usually with tips parallel to the magnetic field. These probes could be scanned both radially and vertically, ie., in an x-y fashion. Single tip probes respond to the wave potential, while double tip probes can be used by subtracting the signals from the two tips, thereby enhancing signals from short electrostatic waves, while rejecting long electromagnetic components. These techniques have been described before with the Princeton L-3 and L-4 devices.[22] Any attempt at reliable absolute calibration of these probes at RF frequencies is fraught with difficulties. Even good calibration in air or vacuum, which was found to be most easily performed with an open strip-line cavity,[23] does not take into account

differences due to plasma sheath effects. Consequently, one desires a different approach, in principle provided by the laser scattering system described next.

C. Laser system

A CO_2 laser scattering system has been built to take advantage of the steady-state ACT-I plasma. Since we desired to study density fluctuations with $k_\perp$ in the range accessible to a CO_2 scattering system while scanning across at least one half of the plasma diameter, we chose a geometry where the high power CO_2 beam traversed the plasma along primarily a vertical chord, allowing essentially radial, or k_x components of $\tilde{E}$ to be observed. A schematic of the setup is shown in Fig. 6.

With the exception of the reentrant cavity design which holds the optical windows and their shutters on the vacuum vessel itself, all optics were mounted on an optical table riding on a motorized cart. This allowed data to be taken while the cart was in motion, and proved very useful when searching for plasma waves localized in radial extent. Mirrors M6 and M7 are attached to stiff aluminum channel arms which extend 75 cm off the table into the reentrant cavities. Lens L2 (4" dia, 215 cm f1), which is 3 meters from the plasma, serves both to focus and cross the high power (solid line) and local oscillator (dashed line) laser beams in the plasma midplane. By displacing mirror M5, the separation between the two beams prior to lens L2 is changed, thereby allowing the crossing (scattering) angle to be scanned. After leaving the plasma, the high power beam is dumped at a power monitor.

The scattering geometry, with the local oscillator beam actually passing though the plasma, rather than some other path outside of the machine, was chosen for ease of alignment. The alignment requirements are fairly stringent for good heterodyne mixing efficiency. The scattered light beam must be colinear with the local oscillator beam to within an angle $\Delta\theta \leq \lambda_o/\pi a_o \approx 1$ mrad, where $a_o = 3.3$ mm is the laser beam waist in the plasma. At the same time, we need angle ($k_\perp$) scanning ability. Consequently, the angle definition and alignment afforded by this choice of beam path was preferred over the minor drawback of running the LO beam through the plasma. Additionally, since two beam paths are nearly identical, phase changes due to mirror vibrations tend to be automatically compensated.[11]

The detector, a photoconductive Ge:Cu semiconductor element 0.5 mm in diameter, is housed in a liquid helium dewar, and is supported by a y-z adjustable platform which sits on an upper level deck (bolted firmly to the main optics table). It has a straight shot at light from mirror M7. The dewar, its battery-powered electronics package and bias supply, are all encased in a copper shield box, having only a 1" diameter hole for light input, and fiber optic leads to carry signals out. In this manner, RF pickup problems were completely eliminated. Low noise 5-250 MHz Trontech preamplifiers with a total power gain of up to 75 db were used. A bandpass filter between preamp stages prevented destruction of the second stage preamp if laser mode-beating occurred. There is a substantial impedance mismatch between the detector and the preamp, which although undesirable because it reduces the signal, is not harmful as long as the detector shot noise (or gain-recombination noise), which is the dominant noise, is itself also reduced in the same fashion by the impedance mismatch. The signal after amplification, never more than 1-2 mV in amplitude, was fed to a Meret MDL-259 wideband (1-140 MHz) fiber optic link to the outside world.

D. Absolute calibration

An important element of this paper lies in the absolute calibration of the scattered laser signal so that lower hybrid power levels can be deduced in the plasma. We will describe the system calibration in detail. The detector is operated with adequate local oscillator power (~100 mW) to insure that the local oscillator induced shot noise (or gain-recombination noise) dominates amplifier noise, Johnson noise, and any pickup from the surrounding environment. We define the receiver noise equivalent power (NEP) as the power per unit bandwidth which gives a power signal to noise ratio (SNR) of unity. For a photoconductor, NEP = $2h\nu/\eta$, where η is the net quantum efficiency.[24] The quantum limit NEP is 3.7×10^{-20} W/Hz, while the best reported values are system NEPs of 1.5×10^{-19} W/Hz.[25] We use a blackbody calibration to find the NEP as a function of freqency f. An interesting feature of this measurement is that the distance of the blackbody from the detector does not enter into the calculation, as long as the solid angle subtended by the blackbody aperture overfills the diffraction limited receiver coherent solid angle $\Omega = \lambda_0^2/A$, where A is the detector surface area. Peyton[26] provides a good treatment, where a solar radiometer was calibrated using this technique, although with a photovoltaic detector. We can

write the power received from a blackbody into the coherent solid angle Ω with correct polarization for heterodyne detection, as

$$P_{bb} = \frac{\alpha\, h\nu\, (2\Delta f)}{\exp\left(\frac{h\nu}{kT} - 1\right)} \quad . \tag{17}$$

where α is an optical transmission factor (in our case 0.43, due to a ZnSe beamsplitter), and because of the double sideband nature of the measurement, we use twice the IF bandwidth Δf. By mixing the local oscillator beam with light from a known temperature "blackbody," we are able to observe the SNR in a given IF bandwidth Δf, using a chopper in the blackbody beam, and locking-in at a 350 Hz chopping rate. The setup is shown in Fig. 7a. An Infrared Industries Model 643 commercial blackbody source at $T = 1283^0$ K with a 1" aperture, corrected for spectral emissivity of the surface was used as the "blackbody." Both low pass and bandpass filters were used after a 65 db power gain front end amplifier, but prior to squaring with an RF crystal detector. This signal was then fed to a Brookdeal lock-in, looking only at the fundamental chopper frequency component, and the output to a strip-chart recorder The SNR was found by alternately blocking and unblocking the blackbody beam, while defining the noise value as 1/3 the peak to peak noise. Time constants were typically 0.3-3.0 sec, with SNRs of 5 to 80. Representative cases are shown in Fig. 8b for three different IF filters.

The signal to noise ratio seen in a given IF bandwidth Δf when observing the chopped blackbody radiation P_{bb} can be written as

$$SNR = \frac{P_{bb}\, (\Delta f\, \tau_1)^{1/2}}{\lambda\, (NEP\, \Delta f)} \quad , \tag{18}$$

where τ_1 is the lock-in post detection time constant, and $\lambda = 2$ takes into account the degradation due to the chopper. Combining Eqs. (17) and (18), we can write the "blackbody" NEP as

$$NEP = \frac{\alpha\, h\nu\, [\Delta f\ \tau_1]^{1/2}}{SNR\ \{\exp(\frac{h\nu}{kT} - 1)\}} \quad . \tag{19}$$

Fig. 8 shows the resulting system NEP as a function of frequency, with the horizontal bars being the Δf used to make each measurement. Apparently "1/f" noise (thought to be contact noise) begins to be a problem below 40 MHz.[27] We did not look higher than 250 MHz, although both the signal and shot noise begin to roll off above 200 MHz. This NEP takes into approximate account the heterodyne mixing efficiency ξ_H,[11] and explicitly includes amplifier noise, since the same amplifiers and similar optics are used here as in the actual experiment. In the blackbody case, a uniform plane wave signal mixes with the Gaussian local oscillator, while in the actual scattering experiment, a matched Gaussian signal mixes with the Gaussian local oscillator beam.

This NEP can be used to relate an observed signal to the scattered laser power P_s. From Eqs. (56-57) of Slusher & Surko,[11] one can see that

$$\frac{< i_{ls}^2 >}{< i_{GR}^2 >} = \frac{\eta \xi_H^2}{2\ h\nu\ \Delta f} \frac{P_{lo} P_s}{P_{lo}} \tag{20}$$

where $< i_{ls}^2 >$ is the mean-square current due to the beat term between the scattered laser power P_s and the local oscillator beam P_{lo}, reduced by the heterodyne mixing efficiency ξ_H. The beat term is $P_{ls} = 2\xi_H (P_{lo} P_s)^{1/2} \cos(\omega t + \varphi)$. By folding ξ_H^2 into the operational definition of NEP, we see that

$$\frac{P_{signal}}{P_{noise}} = \frac{P_s}{NEP\ \Delta f} = \frac{< i_{ls}^2 >}{< i_{GR}^2 >} \quad . \tag{21}$$

Experimentally, for the case of matched Gaussian and local oscillator beams hitting a detector with radius comparable to the focussed beam waist, we expect $\xi_H = 0.6$–0.9. As an indirect measure of this, an Isomet 40 MHz acousto-optic modulator was used to generate a frequency-shifted laser beam of known laser power.[28] This beam was then introduced into the local oscillator beam path via a beamsplitter, and both were focussed in the usual manner on the Ge:Cu detector, producing a signal of 2.2 V/W at the front end of the preamplifier chain. By successively reducing the power to the modulator by over 80 db, the signal was observed to disappear into the shot noise at a level of 2×10^{-18} W/Hz, which is poorer than estimated from the blackbody measurement by a factor of two, suggesting $\xi_H^2 = 0.5$. This is consistent with Cohen,[29] who predicts under ideal conditions of alignment that $\xi_H^2 = 0.95$ for the uniform/Gaussian profile as in the blackbody measurement, but $\xi_H^2 = 0.6$ for the matched Gaussian case above. Naturally, any phase front misalignment on the detector will act to alter ξ_H, usually in a detrimental fashion.[30]

E. Signal processing

At this point we depart from the usual signal to noise formulas,[11,31] and consider the case where there is a coherent narrowband signal and incoherent wideband noise. This is the case of most interest to us, since we look at driven fluctuations at a known frequency ω_0, whereas the dominant noise is gain-recombination noise occurring over a wide bandwidth. The analysis of Smith[32] applies, and a good reference for heterodyne signal to noise considerations is found in Sec. 3 of Sharp *et al*.[33] The signal from the detector was processed in one of three ways, all involving signal enhancement.

If the desired signal maintains phase coherence with the radio frequency pump, we can use a high frequency RF lock-in amplifier, the Princeton Applied Research 5202, for frequencies up to 50 MHz. The lock-in reference signal is simply split off from the RF applied to the antenna on the torus. Then effective noise bandwidths are 10 Hz or less, depending on the lock-in time constant. This technique involves a CW laser, a steady-state plasma, and continuous RF applied to the antenna. An example, using a 50 MHz lower hybrid wave, is shown in Fig. 9a. Accurate measurements of both rms voltage and phase with respect to the pump can be obtained, although the exact gain in SNR as a result of the lock-in is difficult to quantify. However, $\lambda_\perp$ can be very accurately measured as the laser is scanned in radius.

If a somewhat larger scattered signal is available, an HP Spectrum Analyzer can be used as a tuned rms voltmeter, whose IF bandwidth and center frequency is adjustable over a wide range of operating conditions. This technique loses phase information, but does not demand coherence with the applied RF, and can look at frequencies offset from the pump, as well as retaining direct information about the noise level in the IF bandwidth being observed. In a stationary plasma, with steady-state waves, IF bandwidths as small as 1 kHz, but more typically 10 kHz, could be used to reduce the local oscillator noise without reducing the desired signal. Furthermore, by blocking the beam momentarily, the noise contribution due to the root-mean-square LO shot noise could be measured in the absence of signal, as shown in Fig. 9b. The "hash" is not the noise we refer to, but instead we are interested in the quantity denoted as V_x. The signal voltage can then be found by noting that $V_{display} = V_x + V_y = (V_s^2 + V_n^2)^{1/2}$. The hash determines the accuracy of the SNR, but not the SNR itself, and can be arbitrarily reduced by increasing the video time constant. To the extent that the shot noise is the dominant noise, then $V_x = V_n$, and one can relate the desired signal to the observed V_y and V_n. In fact, with Eq. (21), the absolute scattered power can be found from V_s/V_n.

Finally, when the RF or plasma is pulsed, boxcar signal averaging becomes useful. Here the bandwidth of the spectrum analyzer is opened up (up to 300 kHz), while still being used as a tuned rms voltmeter, and its vertical output fed to a PAR Boxcar Integrator. Time resolved measurements can be done, with time resolution of the gate width, while relying on the rapid pulse nature of the RF (or plasma) to obtain good statistics.

IV. EXPERIMENTAL RESULTS

A. Resonance cone detection

We begin by demonstrating LHW cone detection with the CO_2 laser system on ACT-I. We first employ a simple internal grid to excite the wave. In Fig. 10, laser radial scans of a 190 MHz lower hybrid wave (actually an electron plasma wave in this case) are shown. The launching antenna (located radially by the arrow labeled "grid") was 14 cm away toroidally, so that the cone angle θ with respect to the toroidal magnetic field was given by $\Delta r/\Delta z \simeq 1.2/14 = 0.087$. The plasma was cold, $T_i \simeq 0.2$ eV, $T_e \simeq 1$ eV, and the local density inferred from the cone angle was $n_e \simeq 5\times10^{10}$ cm^{-3}. No signal in the plane of the grid is

observed, but instead, the wave is concentrated in the resonance cone. Each trace in Fig. 10 corresponds to a different laser scattering angle, and waves are detected with $k_\perp$ = 20 to 90 cm^{-1}. For $\omega >> \omega_{pi}$, different $k_\parallel$ have $k_\perp$ given by $k_\perp/k_\parallel = \omega_o/\omega$. Since we observe a range of $k_\perp$, we can infer the wave $k_\parallel$-spectrum. Later, Eq. (6) will be used to do this, keeping the ion terms for more accuracy as ω approaches ω_{pi}. The dashed line indicates a corresponding probe trace, which only resolves the cone location. For the top trace, the high power laser beam was blocked, showing the "zero" angle density disturbance seen by the low power local oscillator beam alone. Since the lock-in amplifier and fiber-optic link used here have bandwidths of 50 MHz and 140 MHz, respectively, the 190 MHz signal was first downmixed with a 215 MHz reference oscillator.

To make the experiment more relevant to large device plasmas, we can launch waves from antennas placed on the edge of the plasma in the limiter shadow. Here the LHW must traverse a region similar to that encountered in large toroidal devices, i.e., a zone of large amplitude low-frequency density fluctuations.[3] In addition, the use of a phased array antenna better defines the parallel wavelength than a simple grid. Fig. 11 shows lower hybrid resonance cones detected by CO_2 laser scattering, launched from such an array located two ports (~ 30 cm) toroidally away from the laser location. The density $n_e \sim 1.1\times10^{10}$ cm^{-3} was fairly uniform over the radius r = 2.5 to 5.0 cm, as indicated by the linear increase in wave penetration with frequency. The laser scattering angle was centered at $k_\perp^o = 30$ cm^{-1}. Relative amplitudes between traces in Fig. 11 are not meaningful, since the characteristic antenna impedance is resonant at some frequencies in this range.

However, it quickly became apparent that resonance cone detection was not to be taken for granted. Changing the magnetic field correction coils, the RF power level, the antenna phasing, or the plasma density could eliminate the laser signal entirely, even though a probe might still show a localized signal. The laser is of course $\vec{k}$ selective, and integrates over a vertical chord, whereas the probe responds to a broad range of k and is local. We now proceed to sort out these effects.

The degree of vertical uniformity is important for the laser signal, which is proportional to $\tilde{n}\, L_{eff}$. Fig. 12 depicts a vertical cross section of a lower hybrid wave front, obtained by an x-y scanning probe, two ports away from the antenna. The antenna (at r = 6.5 cm, 12.7 cm tall) hides in the shadow of a vertical limiter, drawn in as the straight line at r = 6 cm. The vertical

exaggeration is 2.5:1. An unused ring antenna conveniently shows up as a blip with a 9-cm radius of curvature, marking the curvature of the outer wall. The six-plate antenna structure ($\pi/2$ phasing) imposes a 5/4 period wave pattern in the radial direction, as expected.[34] In this case, the local midplane density at the cone is low, $n_e \approx 7\times10^9$ cm^{-3}, so that $\omega/\omega_{pi} \approx 3$. At first glance, the wavefront looks very planar, with curvature near the top and bottom indicating lower density at the top than the bottom of the machine. However, on the scale of $\lambda_\perp \approx 3.8$ mm, a phase shift of $\pi/2$ occurs for an x displacement of only 1 mm. To minimize cancellation of laser signal, and maximize the effective scattering length L_{eff}, it is clear that the laser $k_\perp^o$ should be aligned with the wave $k_\perp$ vector in angle, at least to within the spread associated with a finite antenna height L_A in the y-direction, $\Delta k_y \sim 1/L_A$. The general tilt of the wave with respect to vertical is $\approx$ 30 mrad. Assuming that the laser is lined up with this "tilt," then due to the remaining curvature of the wave front at the top and bottom of the antenna, based on a $\pi/2$ relative phase shift, the maximum L_{eff} is estimated to be 6 cm, or half the antenna height. When observing farther away from the launcher, the tilt will get worse (for this profile) and the dominant $\lambda_\perp$ gets shorter as the wave penetrates to higher densities along its trajectory, thereby further reducing L_{eff}. As a further check on the effective laser scattering length, it is observed that insertion of a probe at a distant toroidal location causes changes in the laser signal. In particular, when the laser is located on a LHW resonance cone, scanning a probe into the plasma causes a decrease in the laser signal beginning when the probe is ~ 1 cm into the plasma, moving the cone seen by the laser inwards, indicating a reduction in plasma density from the plasma edge to the cone location as a result of probe insertion. By inserting the probe at different vertical positions, one could see the largest decrease in laser signal with the probe in the plasma midplane, and less to either the top or bottom of the plasma, indicating that the laser signal originates over a several centimeter path length.

Simply aligning the antennas and laser to better than 1° vertically is difficult, let alone controlling the symmetry of the plasma profile. To get around this problem, tilting antennas were built. The limiters, which stick $\approx$ 0.5 cm further into the plasma are left fixed. Fig. 13 shows the effect of tilting the antenna on a lower hybrid laser signal. The "zero" tilt angle denotes only an approximate vertical, due to the small angles employed. Destructive interference, characterized by spatial modulation of the signal

amplitude with wavelength $2\pi/k_\perp^o$ can be seen as the antenna is moved to either side of the optimum tilt angle. The observed full-width, half-max angle is $\Delta\Theta \approx 14$ mrad. For a monochromatic plane wave tilted from vertical, L_{eff} goes as $L_y(\sin(X)/X)$ where $X \equiv (k_y L_y/2)$. Half-max occurs at X=1.89, and since $k_y \approx k_\perp \Theta_{tilt}$, then the fwhm value for $\Delta\Theta$ would give $L_y \approx 16$ cm. This is too large by a factor of ~3 (in particular, it is larger than the antenna $L_A = 12.7$ cm). One infers instead that the wave has a finite spread in k_y, of order $\Delta k_y \sim k_\perp \Delta\Theta \approx 0.5$ cm^{-1}. Indeed, from the geometric effect of finite antenna height, one expects $\Delta k_y \sim 2\pi/L_A \approx 0.5$ cm^{-1}.

The exercise above was significant, because for the purpose of $k_\perp^o$ (magnitude) scanning, where the scattering angle is changed by steering the high power laser beam while leaving the local oscillator beam fixed, one desires that the Δk_y of the wave be broader than the error introduced by changing the direction of $k_\perp^o$. The widest Bragg angle scans which we use cover ~ 10 mrad. With a 2" antenna, angular mismatch due to rotation of the $k_\perp^o$ vector while scanning one beam is not a problem.

Summarizing, if the wave phase front alignment problem relative to the desired $k_\perp^o$ orientation has been eliminated, then the laser signal resonance cone envelope should be free of amplitude modulation with wavelength $2\pi/k_\perp^o$. By tilting the antenna and or plasma (see Fig. 3), this condition could usually be achieved, and is important when inferring wave power spectra.

B. LHW power scaling

Now we consider the scaling of LHW density fluctuations with the applied RF power, detected by CO_2 laser scattering. This measurement is made when the waves are found in well-defined resonance cones, so that the wave energy is known to be travelling into the plasma.

For this experiment we increase the RF power level, and for each level, we scan the laser radially to find the resonance cone. Laser signal corresponding to the peak of the resonance cone (amplitude ~ $\tilde{n}L_{eff}$) is plotted against the square root of the applied RF power in Fig. 14a. In Fig. 14b, the actual laser signals as a function of radius for the different power levels are shown. A shift of the cone position as the power is raised indicates that the wave is perturbing the global plasma parameters. This is seen directly in Fig. 14c, where an ion saturation current monitor in the top of the plasma at a distant fixed position, is seen to change significantly for $P_{rf} > 1/2$ W. The detailed

conditions for this example are shown in Table II. At low powers (<1/2 W), the laser signal is observed to scale linearly with $P_{rf}^{1/2}$, as expected if $\tilde{n}^2 \sim P_{rf}$ (see Eq. 15). The plasma up-down symmetry is very good initially, and the tilt antenna is optimized. Signals could be seen above the noise in a 10 kHz bandwidth with applied RF power as low as 5 mW ($P_\perp < 250\ \mu W/cm^2$). However, maximal signal occurs at only 1.4 W of applied RF power, with no recovery seen even if the power was raised as high as 50 W. This type of absolute reduction in signal eventually with increasing power is characteristic of all LHW laser signals we observed. Switching to different $k_\perp^o$ does not bring the signal back, only lowering the RF power level.

Absolute fluctuation levels provide the key to the problem. Peak density fluctuations (in the range of $k_\perp = 37 \pm 6\ cm^{-1}$) associated with Fig. 14 laser signals, can be estimated to be greater than $3.2 \times 10^8\ cm^{-3}$ (L_{eff}=5 cm) and less than $1.6 \times 10^9\ cm^{-3}$ (L_{eff}=1 cm). The partial $\tilde{n}/n_e$ range from 0.7% to 3.5%, and corresponding partial electric fields, obtained using Eq. (10), from 20 to 90 V/cm. We shall see later that at this laser angle setting, the laser is detecting at best 1/4 to 1/3 of the wave power present. This means that 1 mW/cm^2 to 20 mW/cm^2, or 3 - 60% of the applied RF power can be accounted for in the wave. If all the power were concentrated in the $k_\perp^o$ under observation, then $P_\perp = 35\ mW/cm^2$ would drive $\tilde{n} = 2 \times 10^9\ cm^{-3}$ according to Eq. (15), and an electric field $E_\perp$ =115 V/cm. This would correspond to a wave potential of $\Phi = E_\perp/k_\perp$ =3 V, and a ponderomotive factor $\Delta n/n = E_\perp^2/(8\pi n_e(T_e + T_i)) = 0.03$. The latter is not large, but a factor of 10 increase in RF power would cause significant ponderomotive effects.[35] However, the measured $e\Phi/T_e \sim 1$ is cause for concern, and indicates nonlinear effects may be occurring. In fact, ionization of neutrals by the electron quiver motion in the wave fields is significant. As little as 1 W of RF power was capable of sustaining the plasma discharge at 1% density levels, and several watts were adequate to restrike a discharge that had gone out.

Radial probe scans were made as a function of increasing RF power. They showed the resonance cone moved outward at first, as ionization causes an increased $\bar{n}_e$ along the ray trajectory. Eventually this effect is overcome by ponderomotive depletion of density in regions of intense fields, causing the ray trajectory to penetrate radially further into the plasma than the zero power case. The "superlinearity" in Fig. 14 can then be attributed to a change in L_{eff} with RF power.

An example of the type of steady-state distortion of the plasma profile that can occur is shown in Fig. 15. The initial contours (solid lines) show ion saturation current iso-contours are obtained by an x-y scanning probe in the absence of RF. The central density is ~ 7×10^{10} cm^{-3}, and the plasma is denser in the bottom than the top of the torus. Residual field errors at y = -3 to -4 cm cause a noticeable bulge out near the limiter position. Then an antenna 11 ports away (~150^0) from the probe is switched on at 50 MHz and 10 W of power. The second set of contours (dashed lines) shows the steady-state distortion. Plasma density has increased near the edge and bottom of the torus, and a reduction in density has occurred near the top of the machine. It is interesting to notice that the observed changes are consistent with vortex formation[36] (the toroidal magnetic field is into the page), but the initial density asymmetry precludes a definite answer.

One can see how a given profile can become distorted, perhaps causing an increase in L_{eff} if it was not initially optimal, only to have buckling of wave phase fronts at higher RF power force a net decrease in laser signal, even though $\bar{n}$ may be increasing. Fig. 16 shows LHW (100 MHz) resonance cone amplitude observed with the laser and probe in a 10 kHz bandwidth about the pump frequency, in a plasma similar to that previously described in Fig. 14, except that the initial plasma profile is tilted, and a 5" instead of 2" tall antenna is used. The nonlinearities seen by the laser are not apparent to the probe. As the RF power was raised from 1 - 25 W, the ion saturation current monitor fell by 30%. The probe is positioned two ports from the antenna, while the laser is four ports away. The clear recovery of the laser signal, peaking at $\bar{n}L_{eff} \simeq 1.5\times10^9$ cm^{-2}, occurs with 18 W of applied RF power. We conclude that profile buckling due to asymmetric ionization has occurred. Confirmation of this mechanism for the "superlinearity" is obtained using a gated RF burst (7 μsec pulse) and looking at the laser signal with a 4 μsec window boxcar aperture. The resulting power scaling is strictly linear up to 16 W, or approximately 10 times higher power levels than the steady-state case. Such a short time scale is adequate for local density depletion if ponderomotive effects are important, but not for significant ionization of background neutrals by the wave.

The largest LHW signal recorded thus far in ACT-I with the laser system corresponds to $\bar{n}L_{eff} \simeq 3.1\times10^9$ cm^{-2} at $k_\perp^0 = 38\pm6$ cm^{-1} and f = 100 MHz, using a heterodyne mixing efficiency $\xi = 0.7$. The applied power was 6 W, and the wave

was detected at a local plasma density of 6×10^{10} cm^{-3}, 60 cm away from the launching antenna. Corresponding scattered laser power was $P_s \approx 3\times10^{-13}$ W for an incident laser power of 30 W. The antenna power levels used here are quoted forward minus reflected power, but the antennas tended to work best at certain discrete frequencies, where the reflected power was ≈ 0, even in the absence of plasma. This indicates the Q of the antenna is high, but actual antenna resistive losses in the LHW frequency range were not measured. We conclude that total $\tilde{n}/n$ (maximum values) for LHW range from the 1%-5% level, driven in a narrow frequency band about the pump frequency, beyond which significant nonlinearities occur.

C. LHW $k_\parallel$-spectrum

Determining the actual wave $k_\parallel$-spectrum inside the plasma is of great interest, since the eventual fate of the LHW energy depends strongly on that parameter.[37] Slusher and Surko[6] have inferred the wave $k_\parallel$-spectrum from a waveguide antenna in the Alcator A plasma by parameterizing their data with the line averaged density during an RF pulse. This technique relies upon fixed $k_\perp^o$ measurements made over a range of densities to sample different $k_\parallel$. This type of density scan measurement was done in ACT-I, with the added advantage of local density measurements, and the localization of wave energy in well-defined resonance cones. Additionally, $k_\perp^o$ (laser angle) scans could be made while holding plasma and wave parameters fixed. The two techniques complement each other. The first suffers from possible differences in wave coupling, the effects of changes in other plasma parameters besides density, or changes in laser scattering length as the "density" is changed, while the second suffers from possible laser calibration uncertainties and differences in $\hat{k}_\perp$ direction being sampled as the laser scattering angle is changed. Using both methods together, a reasonable picture of what is happening inside the plasma can be obtained.

We begin by showing a plasma density scan, parameterized by stepwise increases in the ion saturation current monitored at a fixed point in the plasma. Fig. 17 shows laser signals obtained at one $k_\perp^o$ via the lock-in technique described in Sec. III. The antenna plates are phased by $\pi/2$ so $\hat{E}_\parallel$ is in the same direction as $\hat{B}_o$, that is, towards the laser which is 6 ports (~90 cm) away from the antenna. We note here, that probe signals typically show a 2:1 wave amplitude directionality (4:1 in power) when the antenna is

alternately phased to the right or left, using four of the six plates, with the two end plates left floating. The dominant parallel wavelength defined by the antenna geometry should be $\lambda_{\parallel} \approx 5.2$ cm. In this case, the neutral fill pressure was moderate, ($P = 2.2\times10^{-5}$ Torr, gauge), so the ion temperature was $T_i \approx 0.3$-0.4 eV, implying that the waves observed here have $k_{\perp}\rho_i \approx 0.7$. The key features of Fig. 17 are that the resonance cone does indeed move outward with increasing density, and that the signal is either lost, or is at least decreasing for both high and low densities. The ratio of wave frequency to local plasma frequency ranges from $f/f_{pi} \approx 2.3$ at I_{sat}=0.10 to $f/f_{pi} \approx 1.25$ at $I_{sat} = 1.85$. Peak signal occurs at $I_{sat} = 0.5$, corresponding to $f/f_{pi} \approx 1.8$, for an inferred $\lambda_{\parallel} \approx 6.4$ cm. The parallel wavelengths observed here (by inference from the local cone angle) range from 5 cm at the lowest density to 10 cm at the highest.

We shall see later that the reason for a decrease in signal at the shortest parallel wavelengths is due to electron Landau damping. The reasons for a complete loss of signal at the highest density (long parallel wavelengths) are more complex. In principle, the antenna power spectrum should be falling above $\lambda_{\parallel} = 6$-7 cm, while at the same time long parallel wavelengths have a smaller density fluctuation associated with them when carrying the same amount of energy as shorter $\lambda_{\parallel}$. Furthermore, to be sure that the bulk of the wave energy has not shifted to higher $k_{\perp}$, and is therefore simply being missed, several $k_{\perp}^{o}$ need to be monitored simultaneously. Finally, frequency shifts of LHW by low frequency fluctuations may become more important at higher densities. The lock-in technique used here, which looks in a very narrow band about the pump frequency, would miss a frequency shifted wave. The issues pointed out here will be addressed one by one (to the extent this is possible).

The importance of antenna phasing can be verified by performing laser $k_{\perp}^{o}$ scans for identical fixed plasma parameters, in which only the antenna phasing has been changed. Fig. 18 shows peak resonance cone laser signals versus $k_{\perp}^{o}$ for π phasing and $\pi/2$ phasing of a 6-plate antenna. These data were obtained using the spectrum analyzer at a 10 kHz bandwidth, to avoid the frequency constraints set by the lock-in. It is immediately apparent that higher $k_{\perp}$ are excited by π phasing than by $\pi/2$ phasing, and that more energy is directed towards the laser location in the former, than latter case. The resonance cone was at a local plasma density of $n_e = 5.3\times10^{10}$ cm^{-3} and $f/f_{pi} = 2.2$. Other plasma parameters were $B_z = 4.3$ kG, $T_i = 0.6$ eV, $T_e = 2.5$ eV, and the laser was 5 ports from the

antenna structure. The range of $\lambda_\parallel$ corresponding to the observed $k_\perp$ is from 6.5 cm to 2.5 cm, while at the same time $k_\perp \rho_i$ varies from 0.65 to 1.7. The laser geometry does not allow one to look at perpendicular wavenumbers smaller than ~ 25-30 cm^{-1} without losing absolute calibration, due to the fact that the full coherent solid angle of scattered light lies too close to the main beam, and therefore is not entirely collected.

We can see from Fig. 18, that for $\pi/2$ phasing, the peak density fluctuation at $k_\perp^o \approx 32$ cm^{-1} corresponding to $\lambda_\parallel \approx 5$ cm, is approximately as expected, while for π phasing the peak at $\lambda_\parallel \approx 3.6$ cm is longer (compared with 2.8 cm) than simple antenna geometry might suggest. We note that electron Landau damping should (for a thermal distribution) filter the lower hybrid wave for $\omega/k_\parallel \lesssim 3\ V_e$, which is true here for $\lambda_\parallel \lesssim 3$ cm. Consequently, one suspects that the original wave $k_\parallel$- spectrum has been changed by the plasma. Furthermore, even though the density fluctuations peak at $\lambda_\parallel \approx 3.6$ cm ($k_\perp^o \approx 45$ cm^{-1}), most of the wave energy resides towards longer parallel wavelengths, since the power in the wave goes as $P_w \propto \tilde{n}^2/k_\perp^3$.

Going back to the density scan technique used to sweep across $n_\parallel$ while looking at fixed $n_\perp$, the results of an $f = 39.9$ MHz run are shown in Fig. 19. The signals are obtained at local densities ranging from $n_e \approx 2.6\times10^{10}$ cm^{-3} at $f/f_{pi} = 1.4$ for the longest $\lambda_\parallel$, to $n_e \approx 2.5\times10^{9}$ cm^{-3} at $f/f_{pi} = 4.5$ for the shortest $\lambda_\parallel$. Langmuir probe measurements showed T_e varied from 1.2 eV to 0.6 eV over the range above, and $k_\perp \rho_i \approx 0.8$-$0.9$. Since $k_\perp^o$ is held fixed, the plot of $(\tilde{n}L_{eff})^2$ closely resembles the inferred power spectrum, where ω/ω_{pi} variation has been taken into account. This curve peaks for $\lambda_\parallel \approx 3.8$ cm, falling sharply on the right (low density) to a limit of $\lambda_\parallel \approx 2.4$ cm, and falling more gradually on the left (high density) to a limit of $\lambda_\parallel \approx 9.5$ cm. The sharp fall in signal for high $n_\parallel$ is again consistent with $\omega/k_\parallel \approx 3V_e$, or electron Landau damping. However, the rapid decrease in power for small $n_\parallel$ is not as easy to explain. The expected power spectrum for this case is not directly known, but the plate spacing is 1.3 cm, and the size of the antenna structure in the z direction is ~ 7.9 cm, so seeing waves from $\lambda_\parallel \approx 2.4$ cm to 9.5 cm is not unreasonable.

There are a number of inconsistencies between the two (density scan versus angle scan) methods of measurement. The former usually shows less power at high densities for a given $\lambda_\parallel$ than one infers from measurements made by the latter at fixed, but lower, density. It should be noted that an attenuation of LHW signal at high densities, relative to lower densities, has previously been observed in

the Alcator experiment.[6] We will show that density scans to obtain $k_{\parallel}$-spectra (at least in the ACT-I plasma) should not be relied upon to yield an accurate "snapshot" of the $k_{\parallel}$-spectrum as it exists in the plasma for any one set of plasma parameters.

We can confirm that electron Landau damping is occurring by consecutively monitoring different $k_{\perp}^{o}$ values, while scanning the plasma density to sweep over a range of $\lambda_{\parallel}$. Since the wave is launched from one antenna (r=6.5 cm) and observed toroidally a fixed distance away, the wave trajectory will be seen at different radial locations as the density is changed (as in Fig. 17). Consequently, the laser must be scanned radially for each plasma setting to find the resonance cone. Fig. 20a is a composite, showing along each curve the amplitude of 92.5 MHz resonance cones seen by the laser, and the radius at which the cones were found. Each curve represents a different $k_{\perp}^{o}$, while moving along a curve from left to right corresponds to increasing density during the density scan. The local plasma density when the cone was at the minimum radius was $n_e \approx 2.3\times10^{10}$ cm^{-3}, and when the cone was found out at the largest radius, the local density at the resonance cone was $n_e \approx 7.6\times10^{10}$ cm^{-3}. At any given density, the laser signals from any of the four angle settings were observed at the same radius, i.e., the waves were indeed in resonance cones. Therefore, Fig. 20a represents a 4-point $k_{\perp}^{o}$ scan over a continuum of densities, and the intersection of a vertical line with the four curves gives relative magnitudes of various $k_{\perp}^{o}$ components at a specific density (similar to Fig. 18). Any one of the curves yields information of the type shown in Fig. 19. Fig. 20b shows the actual resonance cone signals for each data point on the $k_{\perp}^{o} = 40$ cm^{-1} curve. For densities above the rightmost cone shown, no resonance cones were seen at this frequency for any of the $k_{\perp}^{o}$, at any radius.

Fig. 20a has two interesting features. The first is that the signal decreases at low densities (short $\lambda_{\parallel}$) for each $k_{\perp}^{o}$ at different values of the density. Close inspection reveals that the left-hand fall off in signal occurs at the same $\lambda_{\parallel}$ ($\approx$ 2.1-2.5 cm) for each $k_{\perp}^{o}$. In fact, $\lambda_{\parallel} = 2.3$ cm yields $f\lambda_{\parallel}/3 \approx 7\times10^{7}$ cm/sec $\approx V_e$ for an electron temperature of 1.4 eV. Independent measurements of T_e range from 1.5 to 2.0 eV, depending on the level at which the plasma source was being driven. The second feature is that the laser signal disappears towards high densities at approximately the same density for each $k_{\perp}^{o}$, over the range of $\lambda_{\parallel} \approx 3$-7 cm, near $n_e \approx 8\times10^{10}$ cm^{-3}, or $f/f_{pi} = 1.8$. In particular, signals corresponding to parallel wavelengths that are seen at lower

density are greatly reduced at higher density. This is depicted in Fig. 20c, which takes cone data from r =1.9 cm and r =2.9 cm in Fig. 20a, and plots inferred wave power versus parallel wavelength for the two densities. At $n_e = 5\times10^{10}$ cm^{-3}, ~ 10× more power is observed for $\lambda_\parallel = 5$ cm than at $n_e = 7.5\times10^{10}$ cm^{-3}. This effect is too strong to be explained by the expected reduction in $\tilde{n}$ [see Eq. (15)] at this level of ω/ω_{pi}. Moreover, searching at higher $k_\perp^o$ does not recover a signal.

This apparent high density limit can be circumvented by switching to higher frequencies. In a different instance, a 50 MHz LHW density scan at $k_\perp^o = 40$ cm^{-1} lost signal as $f/f_{pi} \approx 1.4$, or $n_e \approx 4\times10^{10}$ cm^{-3}. Then when the frequency was doubled, to f = 100 MHz, an excellent laser signal could be seen from several antennas to even higher density, $n_e \geq 8\times10^{10}$ cm^{-3}. This verifies that the decrease in signal at 50 MHz was not due to simple tilting or buckling of the plasma profile. In this case, the upper limit in density was not reached, but was probably greater than 1×10^{11} cm^{-3}. What was different about this plasma, was that the low-frequency edge fluctuations, measured by $\delta I_{sat}/I_{sat}$, were less than 10%, and the central region fluctuations less than 4%. This should be compared to 20-30% edge, and over 10% central fluctuation levels for the Fig. 20 conditions. If the effective laser scattering length is somehow being reduced, the laser signal would disappear in the fashion described above. A mechanism which accomplishes this, decreases at higher frequency, and changes the direction of $k_\perp$ of the LHW, is scattering by low-frequency turbulence.

D. LHW scattering by low-frequency fluctuations

It has been known for a number of years, both theoretically and experimentally, that low-frequency density fluctuations (drift waves) can refract and scatter lower hybrid waves. Due to experimental evidence that significant scattering may occur in tokamaks, theoretical efforts to model the scattering have redoubled.[38,39] It has been estimated on Alcator A that the 2.45 GHz LHW passed through several 90° scattering lengths to reach the plasma interior.[6] No resonance cones were observed, and the LHW signal had a broad frequency spread. The low-frequency fluctuation spectral width (~200 kHz) resulted in a several (2-6) MHz frequency width for the detected LHW. An unexplained frequency downshift was also observed.

Driven lower hybrid waves in ACT-I are observed to be scattered by pre-existing low-frequency density fluctuations. The degree of scattering is highly dependent on the level of low-frequency edge fluctuations, and tends to become more severe as the density is raised. Due to the toroidal geometry of ACT-I, and the present scanning capabilities of our probes, it is not possible to directly measure k_y of the drift waves, or determine their mode number, as was done previously in linear devices with similar plasma parameters.[20] However, useful estimates can still be made. We also point out that interesting measurements in the WIIa stellerator have recently been performed characterizing its low-frequency turbulence, although under conditions of even higher turbulence than in ACT-I.[40]

Experimentally, due to the low absolute $\tilde{n}$ associated with driven waves in ACT-I, the laser needs as high a degree of frequency and spatial coherence (with planar wavefronts) as is possible to see good resonance cone signal. The presence of a layer of low-frequency (~20-100 kHz), high amplitude ($\delta n/n$ = 0.1-0.3) edge fluctuations, usually 1-2 cm thick in the radial direction, can scatter the LHW on its way to the plasma center, thereby reducing the laser signal.

In the majority of cases observed, we could either see a clean, narrow-frequency laser signal, corresponding to a nonscattered LHW resonance cone, or no laser signal at all, even though a probe would indicate some form of cone was present. Fig. 21a shows the frequency spectrum of an excellent "unscattered" LHW laser signal. However, on a few occasions where the $\hat{k}$ of the scattered wave happened to line up with the direction preferred by the laser, both the pump frequency and frequency-shifted LHW could be seen simultaneously when the laser looked at the resonance cone. This is shown in Fig. 21b, where a 35 kHz red-shifted signal is seen, in addition to an unshifted peak. In this instance, a probe detected both an up- and down-shifted ($f_o \pm 35$ kHz) signal, caused by a fairly coherent 35 kHz drift wave. Another more severe case is shown in Fig. 21c, exhibiting both a sharp component and a broader, slightly asymmetric "base." There is no observed threshold with RF power for these effects, and they appear to be linear phenomena. On one occasion, the laser picked up only signal from a broad low amplitude red-shifted wave, with no peak at all at the center frequency, even though a probe showed a strong component at that frequency. The point to remember is that the laser is $\hat{k}_\perp$ selective.

Recognizing that both coherent and turbulent high level drift waves are present in the ACT-I device, especially near the edge of the plasma where gradients are large, it is difficult to define a scattering length. Nevertheless, theory predicts that the scattering length goes logarithmically to zero as the LHW perpendicular group velocity goes to zero when the wave approaches a mode conversion point or resonance. Using Ott's[21] formula for a 90° scattering length ℓ_s, in the limit that $k_\perp^2 >> \zeta_o^2$, where ζ_o is a characteristic drift wave wavenumber, then

$$\ell_s = \frac{\pi^{3/2}}{4} \frac{\left[k_\perp^2 v_{g\perp}^2 \left(\frac{\partial D}{\partial \omega}\right)^2 \right]}{\zeta_o \left|\frac{\delta n}{n}\right|^2 \left[1 + \frac{3}{2}\left(\frac{\omega_{pe}^2}{\omega \Omega_e}\right)^2 \frac{\zeta_o^2}{k_\perp^2} \right]} \quad . \tag{22}$$

Using the cold LHW dispersion relation, one can estimate for $\omega/2\pi = 100$ MHz, $n_e = 2\times10^{10}$ cm^{-3}, $k_\perp = 20$ cm^{-1}, $\zeta_o = 10$ cm^{-1}, and $\delta n/n = 0.1$ that $\ell_s \approx 30$ cm, or that $\ell/\ell_s = .05$, where $\ell \approx 1.5$ cm is the thickness of the turbulent layer. Good resonance cones would be seen here. The second term in the denominator of Eq. (22), which is the $\hat{E}\times\hat{B}$ coupling term, is smaller than 1 and not significant. However, with $n_e = 5\times10^{10}$ cm^{-3}, the second term dominates, and $\ell/\ell_s = 0.15$. If in fact $\delta n/n = 0.3$, we see that ℓ/ℓ_s quickly becomes of order one. No resonance cones would be seen by the laser in this case.

Probe data actually suggest that $\zeta_o/k_\perp \sim 1$ for the scattered LHW, although the weakest link in our picture is the magnitude of ζ_o. Fig. 22 is a transitional case, where scattering is significant, but resonance cones still survive. Fig. 22a shows radial probe scans using a spectrum analyzer as a narrow band tuned voltmeter, for a sequence of frequencies offset from the pump frequency. The probe is two ports away from a π-phase antenna. We first notice that a good resonance cone remains at $\Delta f = 0$, i.e., at the pump frequency. The initial pump frequency width was less than 100 Hz. However, both to the red and blue sides, frequency-shifted waves are observed in broadened "cones" which do not penetrate in as far radially as the main cone. This is consistent with a simple rotation of the original k_x out of the midplane when it was scattered by a drift wave k_y component near the plasma edge. The greater the frequency offset, the farther behind the main cone one finds the peak amplitude of the

frequency-shifted LHW. The plasma profile is shown in Fig. 22b, indicating a hefty 30% edge fluctuation. Fig. 23a shows the corresponding low-frequency spectrum, which consists of coherent drift waves at multiples of 25 kHz, superimposed on an unresolved background extending out to ~100 kHz or more. Fig. 23b shows the LHW power spectrum in this case, integrated over radius. The ratio of frequency-shifted to unshifted waves is 5:1. Furthermore, an asymmetry (more signal blue shifted than red) is readily apparent, and is consistent with an offset in frequency of the same magnitude as the large 25 kHz drift wave seen in the low-frequency spectrum. We note that a simple mechanism exists to generate a frequency asymmetry in the scattered LHW detected by the probe. All that is required is an initial asymmetry in the amplitude of LHW launched from the face of the antenna, as might be caused by an initial plasma vertical density gradient. In the presence of a preferred direction for the drift waves, a LHW which is scattered up or down will have an opposite sign to its frequency shift. Then a probe in the midplane, which detects LHW's which were scattered both up and down from their initial y coordinates, will display differing amplitudes for the up-or down-shifted waves. A nonlinear mechanism is not required, and indeed, no power threshold is observed for the scattered cones described above.

V. SUMMARY

In this article we have reported the observation of lower hybrid wave resonance cones using the technique of CO_2 laser scattering in a laboratory plasma. Resonance cones may be present, but go undetected if the plasma profile and laser scattering geometry are not well-controlled. Curvature or tilt of the LHW phase fronts are shown to be deleterious to cone detection. The unique ability of continuous radial scanning for the CO_2 laser was crucial to finding the LHW cones as plasma parameters were changed. The techniques for absolute calibration of the laser system were presented in detail, as well as various types of signal processing.

The maximum LHW cone signals were in the range of $\tilde{n}/n \approx 0.01$-0.05. Scaling of laser signal with applied RF power becomes nonlinear as plasma profiles change due to ionization of background neutrals, thereby distorting the initial profile, and changing the effective laser scattering length. In fact, the largest uncertainty in making absolute density fluctuation estimates here, is the uncertainty in the effective laser scattering length.

The lower hybrid wave $k_{\parallel}$-spectrum was measured in the plasma by combining laser angle scans at fixed plasma density with plasma density scans at fixed laser scattering conditions. The filtering effect of electron Landau damping was seen directly, and at high densities the wave power in the resonance cone was greatly reduced from that observed at the same $k_{\parallel}$ at lower densities. This reduction in wave power could not be accounted for by the approach to ω_{pi} alone. Instead, it was observed to be associated with increased scattering by low-frequency fluctuations occurring near the edge of the plasma. Switching to higher LHW frequency for a given plasma condition did indeed allow the observation on resonance cones at yet higher densities. These results are of interest to present attempts at driving toroidal current with high power, directed LHW. Destruction of resonance cones, by scattering of the lower hybrid waves, will reduce LHW current drive efficiency. The value of the ACT-I experiment has been to operate in a transitional regime, where cones are still present, but the effects of scattering can be observed.

ACKNOWLEDGMENTS

The authors would like to thank J. Taylor and W. Kineyko for their excellent technical assistance, and to acknowledge useful discussions with C. Surko, R. Slusher, N. Bretz, P. Andrews, R. Motley, and L. Chen. This work was supported by US Department of Energy Contract No. DE-AC02-76-CHO-3073.

REFERENCES

* Present address: Los Alamos National Laboratory, Los Alamos, NM 87545.

[1] S. Bernabei, C. Daughney, P. Efthimion, W. Hooke, J. Hosea, F. Jobes, A. Martin, E. Mazzucato, E. Meservey, R. Motley, J. Stevens, S. von Goeler, and R. Wilson, Phys. Rev. Lett. 49, 1255 (1982).

[2] J. J. Schuss et al., Nucl. Fusion 21, 427 (1981).

[3] C. M. Surko and R. E. Slusher, Phys. Rev. Lett. 37, 1747 (1976).

[4] R. W. Motley, F. J. Paoloni, S. Bernabei, and W. M. Hooke, Rev. Sci. Instrum. 49, 1143 (1978).

[5] C. M. Surko et al., Phys. Rev Lett. 43, 1016 (1979).

[6] R. E. Slusher and C. M. Surko, Phys. Fluids 25, 457 (1982).

[7] E. Zilli, Int. J. Infrared Mil. Waves 2, 713 (1981).

[8] K. L. Wong, M. Ono, and G. A. Wurden, Rev. Sci. Instrum. 53, 409 (1982).

[9] J. Sheffield, Plasma Scattering of Electromagnetic Radiation, (Academic Press, New York, 1975).

[10] C. M. Surko, R. E. Slusher, D. R. Moler, and M. Porkolab, Phys. Rev. Lett. 29, 81 (1972).

[11] R. E. Slusher and C. M. Surko, Phys. Fluids 23, 472 (1980).

[12] C. M. Surko and R. E. Slusher, Science 221, 817 (1983).

[13] T. H. Stix, The Theory of Plasma Waves, (McGraw-Hill, New York, 1962).

[14] B. D. Fried and S. D. Conte, The Plasma Dispersion Function, (Academic Press, New York, 1961).

[15] G. A. Wurden, K. L. Wong, F. Skiff, and M. Ono, Phys. Rev. Lett. 50, 1779 (1983).

[16] R. K. Fisher and R. W. Gould, Phys. Fluids 14, 857 (1971).

[17] T. H. Stix, Phys. Rev. Lett. 15, 878 (1965).

[18] M. Ono, K. L. Wong, and G. A. Wurden, Phys. Fluids 26, 298 (1983).

[19] G. A. Wurden, M. Ono, and K. L. Wong, Phys. Rev. A. 26, 2297 (1982).

[20] P. M. Bellan and K. L. Wong, Phys. Fluids 21, 592 (1978).

[21] E. Ott, Phys. Fluids 22, 1732 (1979).

[22] P. M. Bellan and M. Porkolab, Phys. Fluids 19, 995 (1976).

[23] I. G. Brown and V. Shepherd, Plasma Phys. 9, 741 (1967).

[24] M. C. Teich, Proc. IEEE 56, 37 (1968).

[25] F. R. Arams, E. W. Sard, B. J. Peyton, and F. P. Pace, IEEE J. Quantum Electon. QE-3, 484 (1967).

[26] B. J. Peyton et al., IEEE J. Quantum Electron. QE-11, 569 (1975).

[27] J. H. Massig, Phys. Lett. 66A, 207 (1978).

[28] R. W. Dixon and E. I. Gordon, Bell Syst. Tech. J. 46, 367 (1967).

[29] S. C. Cohen, Appl. Opt. 14, 1953 (1975).

[30] T. Takenaka, K. Taneka, and O. Fukumitsu, Appl. Opt. 17, 3466 (1978).

[31] E. Holzhauer and J. H. Massig, Plasma Phys. 20, 867 (1978).

[32] R. A. Smith, Inst. of Electrical Engineers Proc. 98, 43 (1951).

[33] L. E. Sharp, A. D. Sanderson, and D. E. Evans, Plasma Phys. 23, 357 (1981).

[34] P. M. Bellan and M. Porkolab, Phys. Fluids 17, 1592 (1974).

[35] J. R. Wilson and K. L. Wong, Phys. Fluids 23, 566 (1980).

[36] R. W. Motley, Phys. Fluids 23, 2050 (1980).

[37] F. J. Paoloni, R. W. Motley, W. M. Hooke, and S. Bernabei, Phys. Rev. Lett. 39, 1081 (1977).

[38] P. T. Bonoli and E. Ott, Phys. Fluids 25, 359 (1982).

[39] P. L. Andrews and F. W. Perkins, Phys. Fluids 26, 2537 (1983).

[40] G. Böhm, H. Schlüter, and L. Schmitz, Plasma Phys. 25, 911 (1983).

FIGURE CAPTIONS

FIG. 1 Schematic of the laser/wave scattering geometry. The scattering angle θ_s is defined by the intersection angle of a low power reference beam, and a high power main beam ($\hat{k}_o$, $\hat{E}_{inc}$), so that the scattered wave vector, denoted by $\hat{k}_s$, leaves colinear with the reference beam. Ideally, the plasma wave wavefronts would be vertical ($\theta_{tilt} = 0$).

FIG. 2 Top view of the 28-chamber torus showing typical antenna, laser, and probe toroidal locations. Side limiters at four toroidal locations provide shadowing for RF antennas.

FIG. 3 Optimization of plasma ion saturation current profiles for best vertical uniformity, by varying the current in magnetic field correction coils.

FIG. 4 Typical electron density and low-frequency density fluctuation profiles over the outer half of the torus, where wave studies are performed.

FIG. 5 Six-element lower hybrid wave array antennas. (a). Simple knife edge configuration. (b). Bent plate, vertically tilting configuration, 12.7-cm tall.

FIG. 6 Schematic of laser scattering system and access to the plasma. An RF probe can be scanned across the same toroidal location as the laser for comparison purposes.

FIG. 7 Blackbody calibration of heterodyne detector. (a). Optical layout used to introduce blackbody radiation colinear with the local oscillator beam. (b). Typical chart recorder traces, showing the blocked and unblocked blackbody signal, used to determine NEP as a function of IF frequency.

FIG. 8 System NEP calibration curve versus intermdediate (IF) frequency. Peak efficiency referred to the quantum limit is 5%.

FIG. 9 Two types of signal processing. (a). Laser signal obtained with lock-in amplifier. The number of phase oscillations is greater than actually present in the wave packet, dependent on the ratio $a_o/\lambda_\perp$. (b.) Same signal acquired with spectrum analyzer. No phase information is retained, but the shot noise level can be found explicitly by blocking the local oscillator beam momentarily.

FIG. 10 Laser radial scans of a grid-launched 190 MHz lower hybrid wave at four different $k_\perp^o$ settings. The grid was located 14 cm toroidally away from the laser location.

FIG. 11 Resonance cone behavior observed by CO_2 laser scattering. The lower hybrid waves were launched from an antenna at the outside edge of the plasma.

FIG. 12 Horizontal cross section showing the LHW phase front detected by multiple scans of a floating probe. The effective laser scattering volume will be much less than the antenna height due to phase front curvature.

FIG. 13 Lower hybrid wave laser signal ($f = 50$ MHz, $\pi/2$ phasing towards the laser location, which is four ports away toroidally) as a function of antenna tilt angle. Destructive interference occurs to either side of the optimum angle.

FIG. 14 Power scaling of a 100.7 MHz lower hybrid wave laser signal. (a). Laser signal is linear with $P_{RF} < 1/2$ W. (b). Actual resonance cones as power was increased. Laser signal could be seen down to 5 mW of applied RF power. (c). Remote ion saturation current monitor, showing global plasma changes for higher powers.

FIG. 15. Two-dimensional ion saturation current contours of the steady-state plasma in the absence (solid lines) and presence (dashed lines) of RF power. The presence of a high level 50 MHz lower hybrid wave launched from an antenna in the limiter shadow at $r = 6.5$ cm has distorted the equilibrium profile.

FIG. 16 Laser and probe signals corresponding to peak resonance cone amplitudes as a function of applied RF power. Nonlinearities in the laser signal are not seen by the probe.

FIG. 17 50 MHz LHW laser resonance cone signal using lock-in detection, disappearing at fixed $k_\perp^0$ as the ion saturation current (density) is raised.

FIG. 18 Laser scattering angle scans with fixed plasma parameters for π and $\pi/2$ phasing. Detector shot noise amplitude was 1 unit in a 10 kHz bandwidth. More energy is put into higher $k_\perp$ components with π phasing than $\pi/2$ phasing.

FIG. 19 Results of a density scan at fixed $k_\perp^0$, where locally determined density values were used to assign $n_\parallel$ values to the observed f = 39.9 MHz LHW resonance cones. The decrease in laser signal for high $n_\parallel$ is caused by electron Landau damping.

FIG. 20 Density scan for four different laser scattering vectors, while monitoring the resonance cone at 92.5 MHz. (a). Amplitude of resonance cones seen by the laser, and the radial location where they were found. Each data point corresponds to one machine operating condition. (b). Actual laser data for $k_\perp^0 = 40\ cm^{-1}$, showing the resonances cones shifting outward as the density is raised. (c). Lower hybrid wave power spectrum chosen for two density cases from above, showing that the wave is attenuated at high densities relative to lower densities.

FIG. 21 Lower hybrid wave laser signal frequency spectra on linear vertical scales, for three cases. (a). Only the unshifted pump frequency is seen. (b). A red-shifted 35 kHz sideband in addition to the pump. (c). Severe frequency scattering in addition to a remnant signal at the pump frequency. If the laser beam is blocked, the spectrum analyzer gives a straight line in all three cases.

FIG. 22 Low frequency scattering of a LHW resonance cone. (a). Probe data showing that the LHW scattered by low-frequency fluctuations lags behind the unscattered resonance cone. Frequency offsets from the central frequency

show broadened, lagging cones. (b). Plasma profile information for this case, given by ion saturation current magnitude and fluctuation traces.

FIG. 23 (a). Low frequency spectrum causing the scattering seen in the previous figure. Coherent drift waves are seen at 25, 50, and 75 kHz. (b). Power spectrum of the lower hybrid wave, integrated over radius, obtained from Fig. 22a, showing frequency scattering out of the pump, a ratio ~ 5:1 scattered to unscattered power.

Table I Range of plasma and wave parameters over which the ACT-I experiment is usually operated.

(1) $T_e > T_i$

(2) $\omega \ll \omega_{pe}$, ω_{ce}

(3) $k_\perp/k_\parallel \gg 1$

(4) $\omega/(k_\parallel V_e) = 3 - 100$ where $V_e \equiv (2T_e/m_e)^{1/2}$

(5) $k_\perp \rho_c = .01 - .1$

(6) $k_\perp \rho_i = .05 - 5$ where $\rho_i \equiv V_i/\omega_{ci}$

(7) Multispecies H_1^+ , H_2^+ , and H_3^+ .

Table II. Wave, plasma, and laser scattering conditions for the optimized lower hybrid wave power-scaling case in Fig. 14.

Wave: $f = 100.7$ MHz , frequency.

$r = 1.7$ cm , radius at coax location.

20 cm^2 , antenna area for 2" tall antenna.

= 0 reflected power, driving #3 plate while shorting #4 plate.

Plasma: (RF off).

$n_e = 4.3 \times 10^{10} cm^{-3}$, $f_{pi} = 39$ MHz .

$T_e = 1.8$ eV, $T_i = 1.2$ eV .

$P = 9 \times 10^{-6}$ Torr (gauge) hydrogen .

$B = 4.34$ kilogauss .

Correction coils (15 Amps top, 0 Amps bottom), "vertical plasma" .

Laser: 28 Watts high power beam.

$k_\parallel = 37$ cm^{-1} .

$\Delta k_\perp = 6$ cm^{-1} .

$\Delta f = 10$ kHz, spectrum analyzer .

Toroidally 5 ports from the antenna .

#83X1408

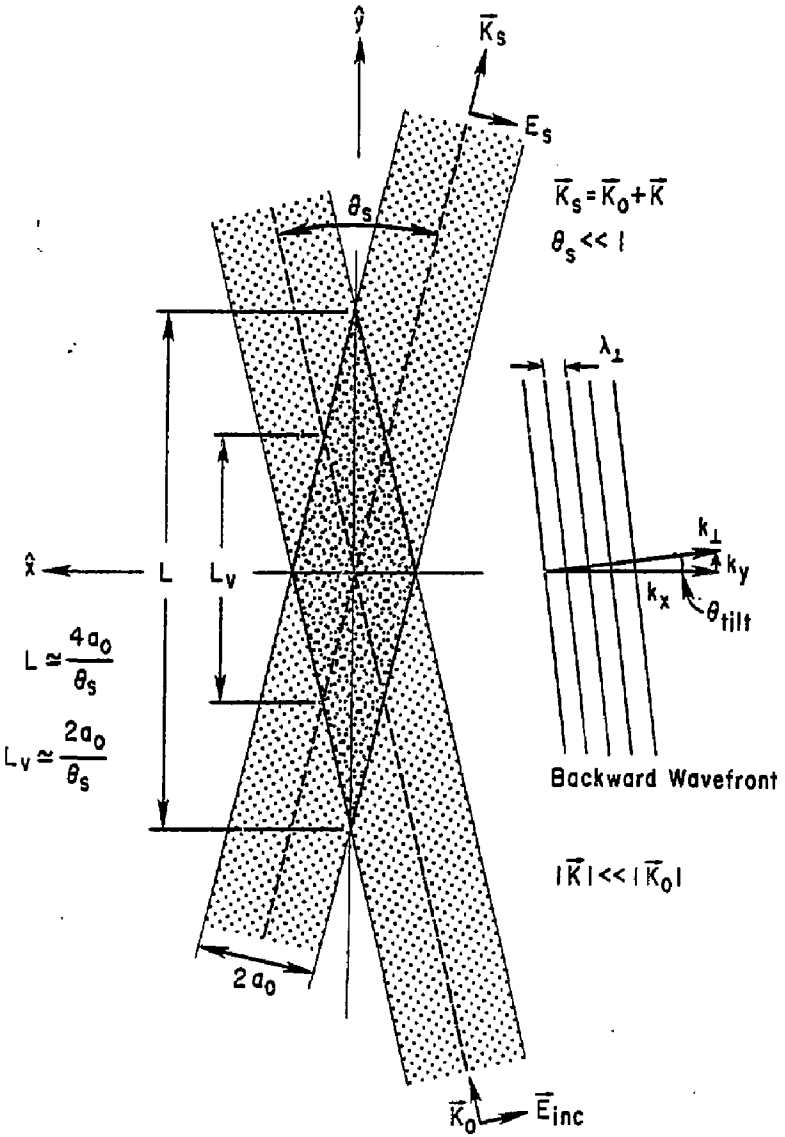

Fig. 1

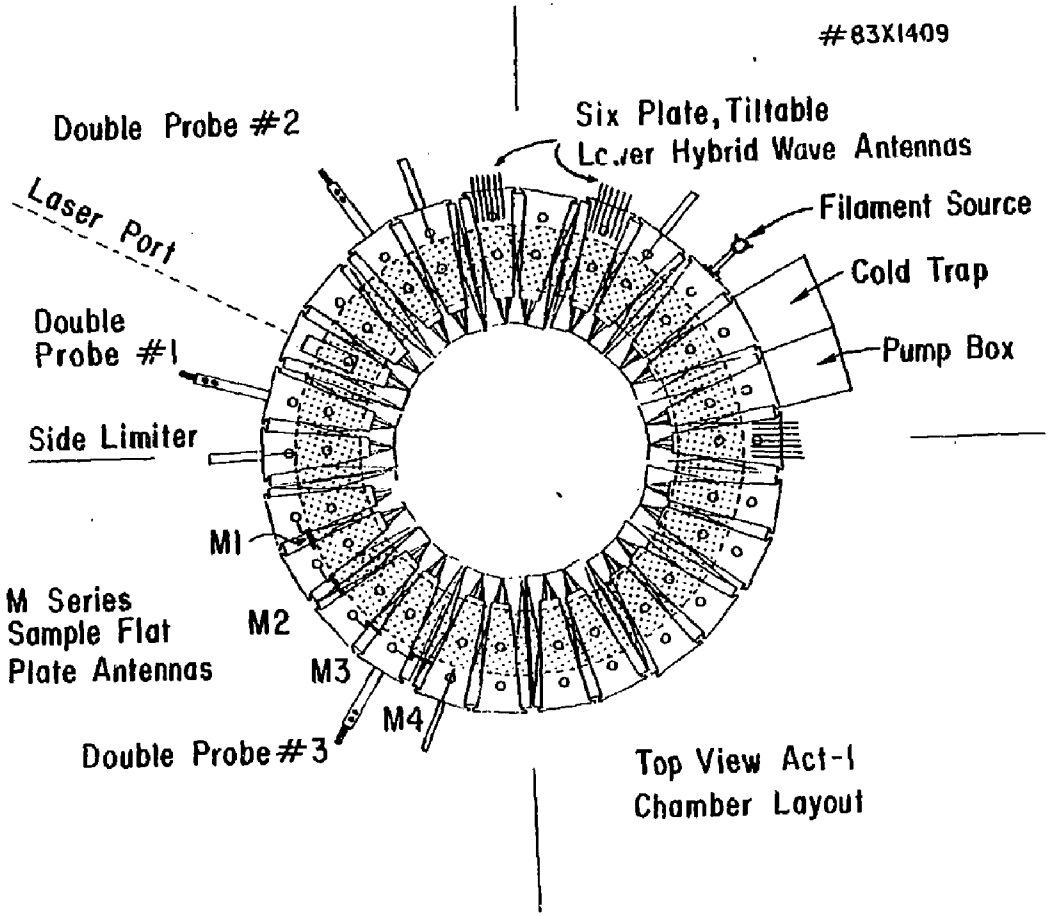
#83X1409
Double Probe #2
Six Plate, Tiltable
Lower Hybrid Wave Antennas
Laser Port
Filament Source
Cold Trap
Double
Probe #1
Pump Box
Side Limiter
M1
M Series
Sample Flat
Plate Antennas
M2
M3
M4
Double Probe #3
Top View Act-1
Chamber Layout

Fig. 2

#83X1397

Effect of Correction Coil on Plasma Profile

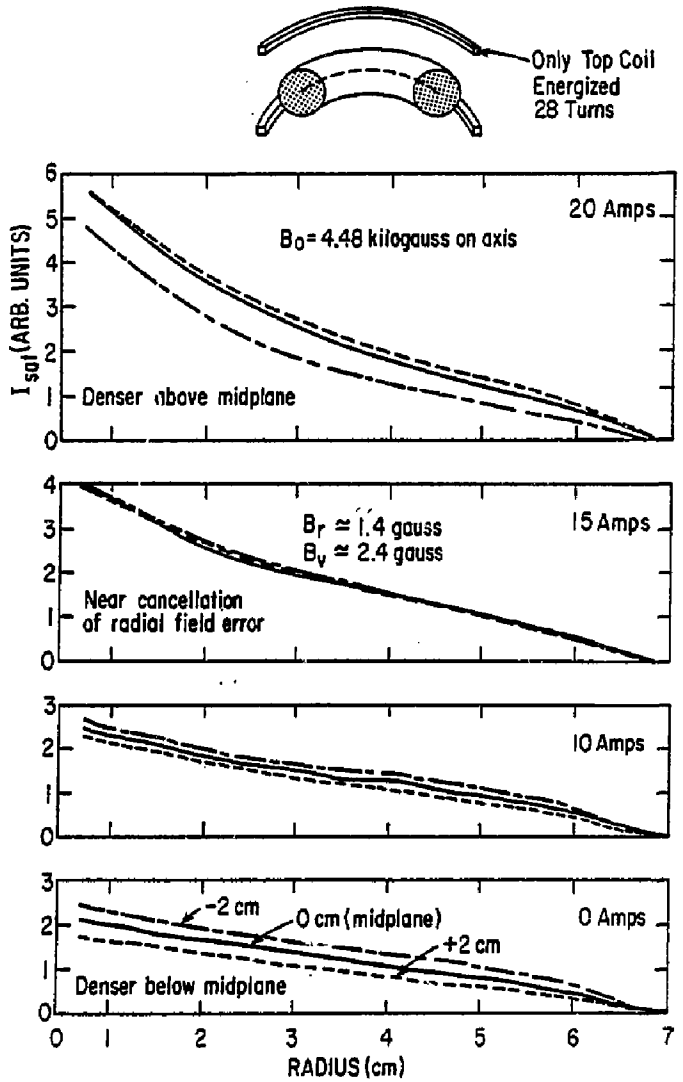

Fig. 3

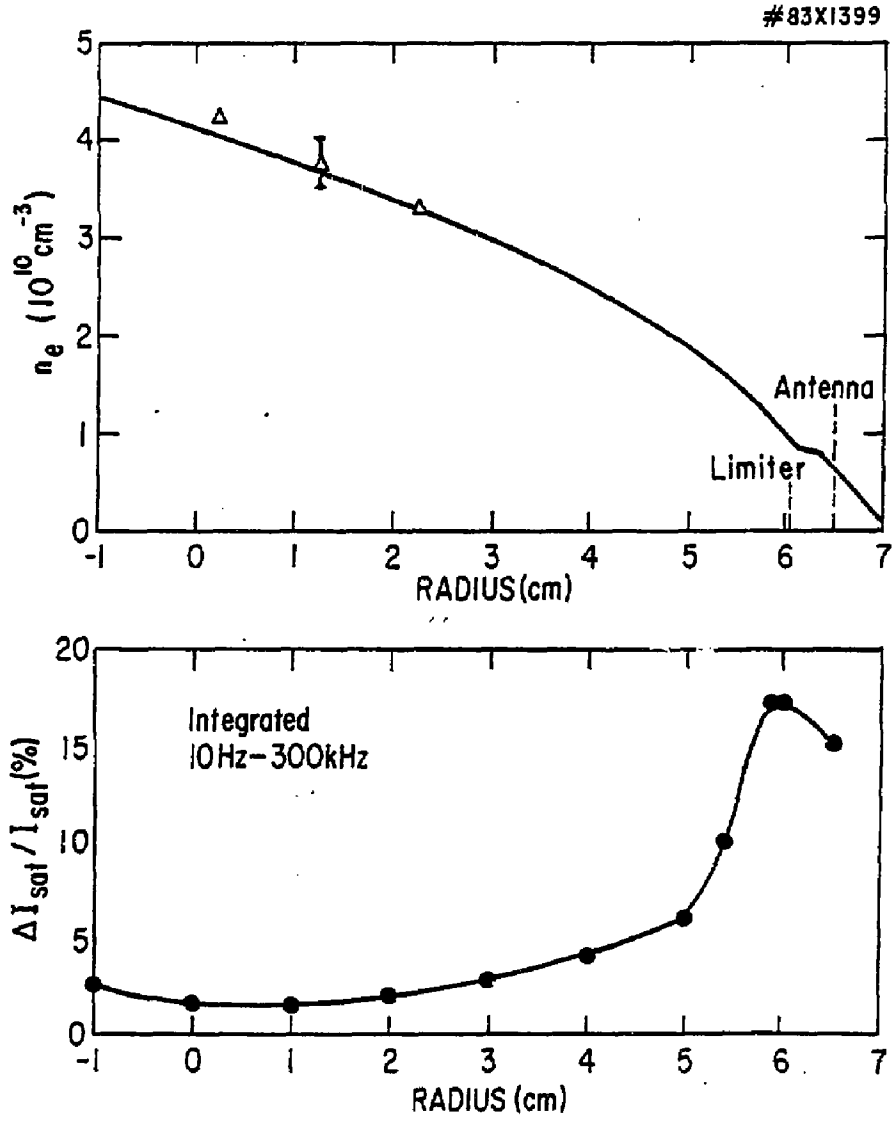
#83X1399
n_e (10^{10} cm^{-3})
RADIUS(cm)
Antenna
Limiter
$\Delta I_{sat} / I_{sat}$(%)
Integrated
10Hz-300kHz
RADIUS (cm)

Fig. 4

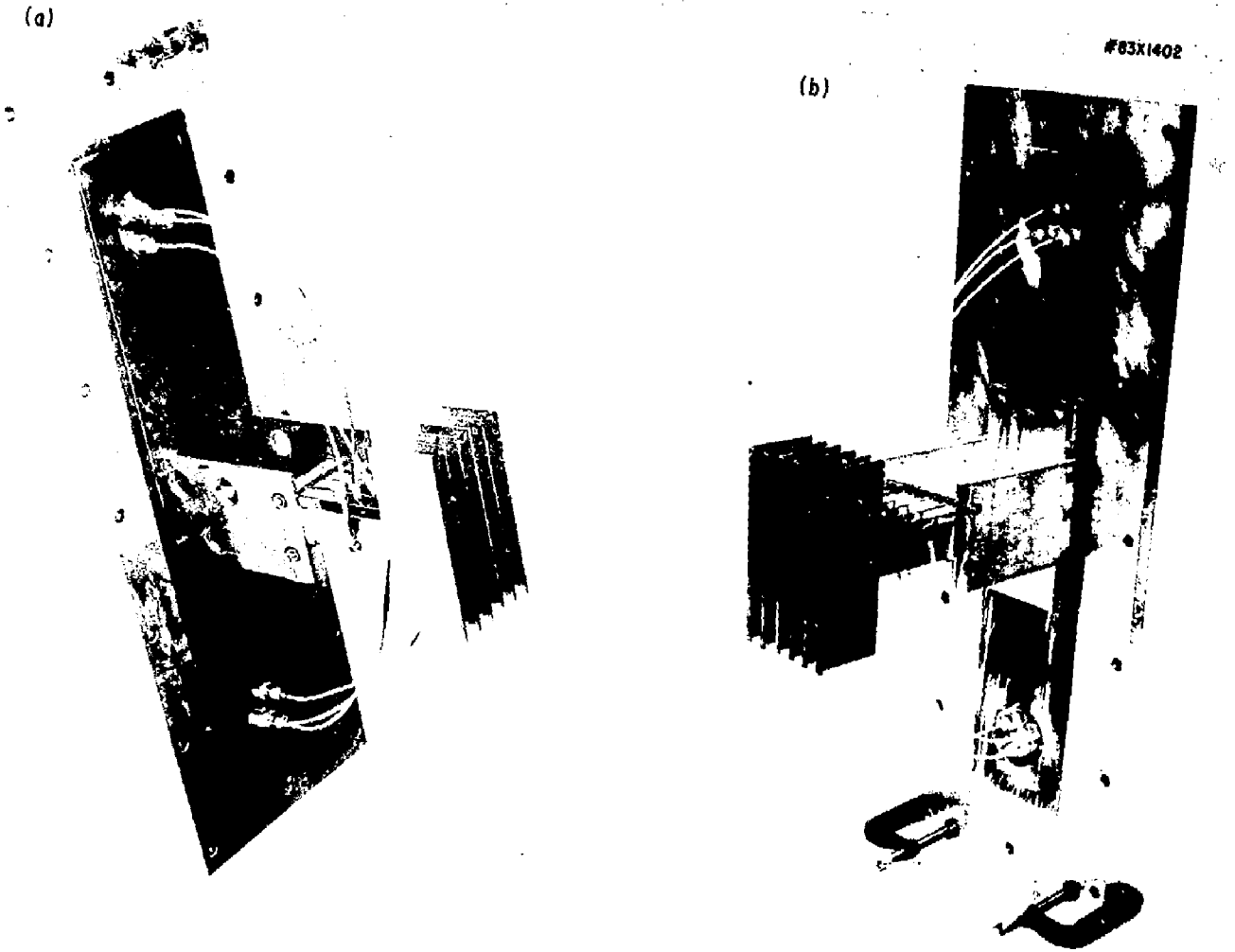

Fig. 5

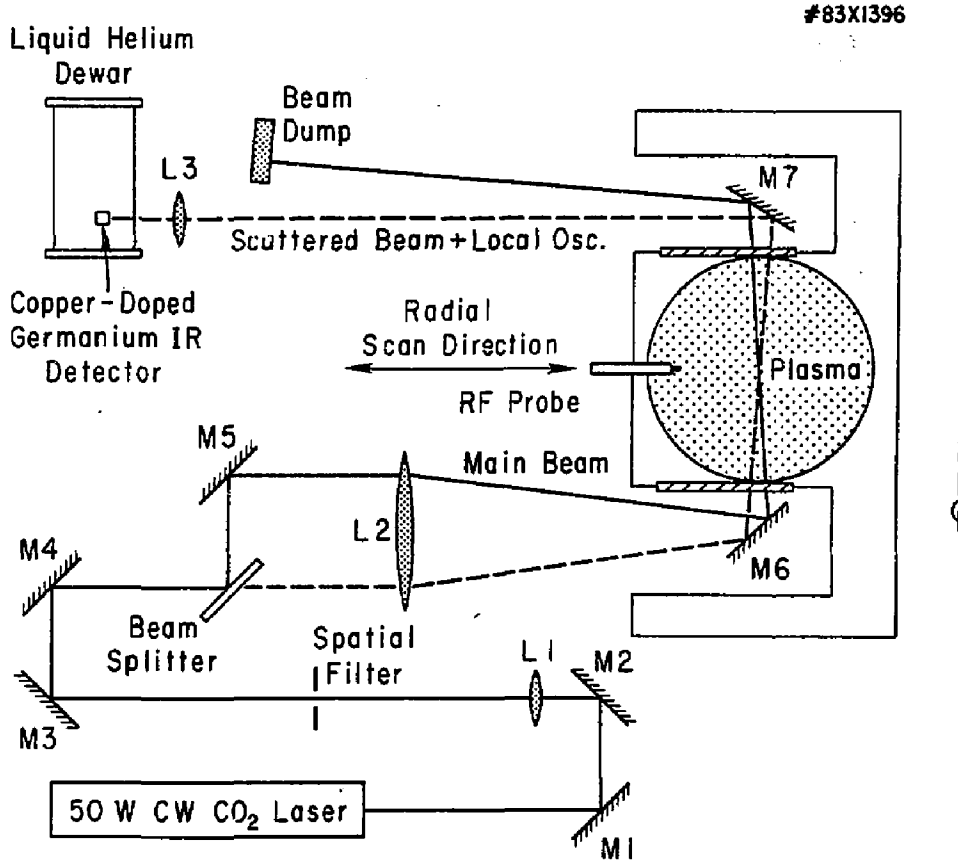
#83X1396
Liquid Helium
Dewar
Beam
Dump
L3
M7
Scattered Beam+Local Osc.
Copper-Doped
Germanium IR
Detector
Radial
Scan Direction
RF Probe
Plasma
M5
Main Beam
L2
M4
M6
Beam
Splitter
Spatial
Filter
L1
M2
M3
50 W CW CO_2 Laser
M1

Fig. 6

#83X1394

BLACKBODY CALIBRATION

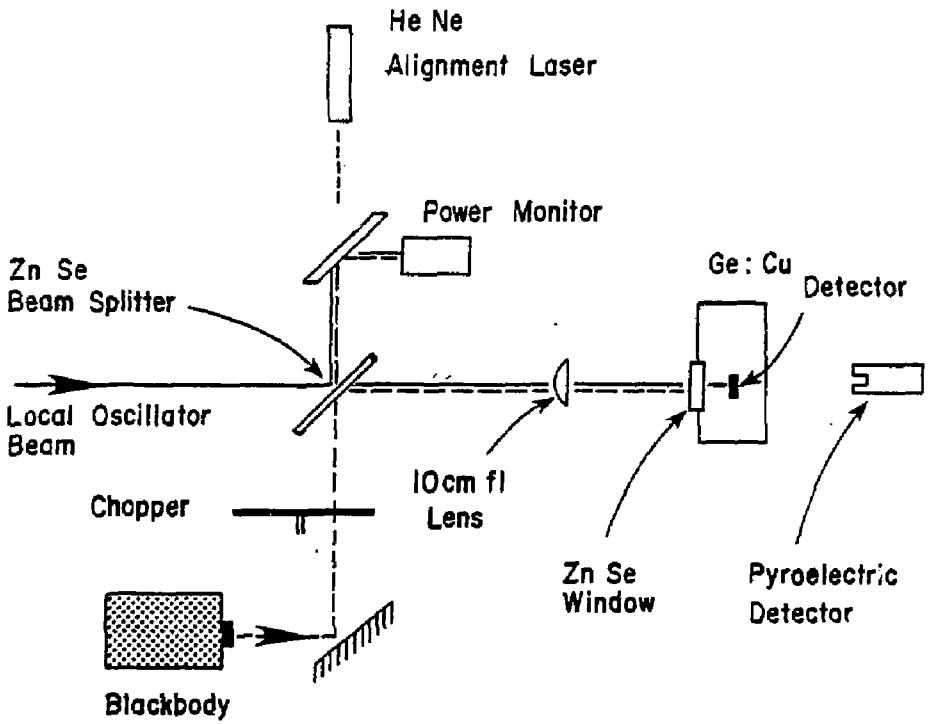

Fig. 7a

#83X1393

Blackbody Calibration

Lock-In Voltage Output, Proportional To Power

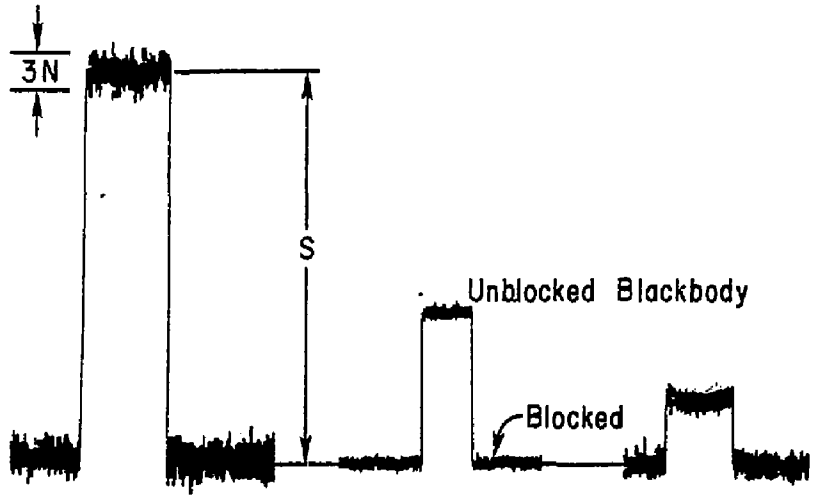

IF Filter: 250 MHz Low Pass	Filter: 143-232 MHz Bandpass	Filter: 50 MHz Low Pass
Integration Time $\tau_1 = 0.3$ sec		
$N \equiv 1/3$ P-P Value		
$(\Delta f \tau_1)^{1/2} = 8.7 \times 10^3$	$(\Delta f \tau_1)^{1/2} = 5.2 \times 10^3$	$(\Delta f \tau_1)^{1/2} = 3.9 \times 10^3$
$S/N \simeq 32$	$S/N \simeq 32$	$S/N \simeq 9$
NEP $= 1.1 \times 10^{-18}$ W/Hz	NEP $= 7 \times 10^{-19}$ W/Hz	NEP $= 2 \times 10^{-18}$ W/Hz

Fig. 7b

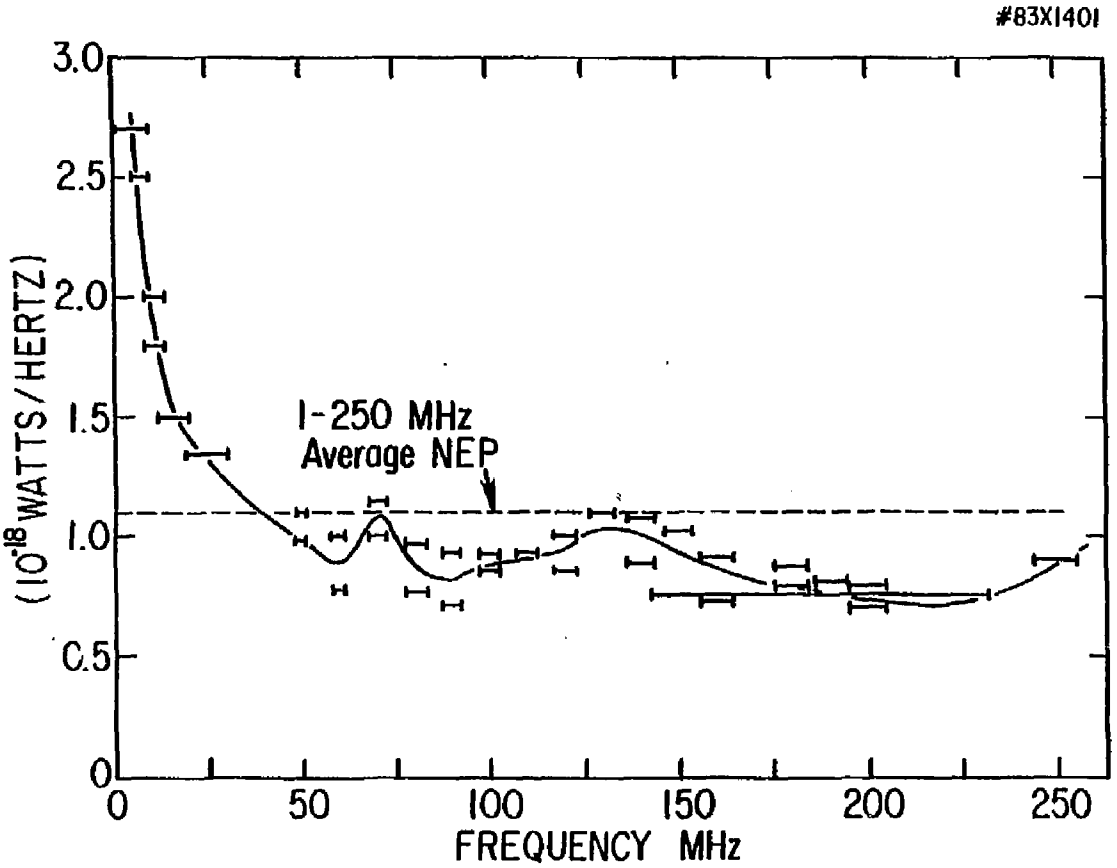
#83X1401
3.0
2.5
2.0
1.5
1.0
0.5
0
(10⁻¹⁸ WATTS/HERTZ)
1-250 MHz
Average NEP
0
50
100
150
200
250
FREQUENCY MHz

Fig. 8

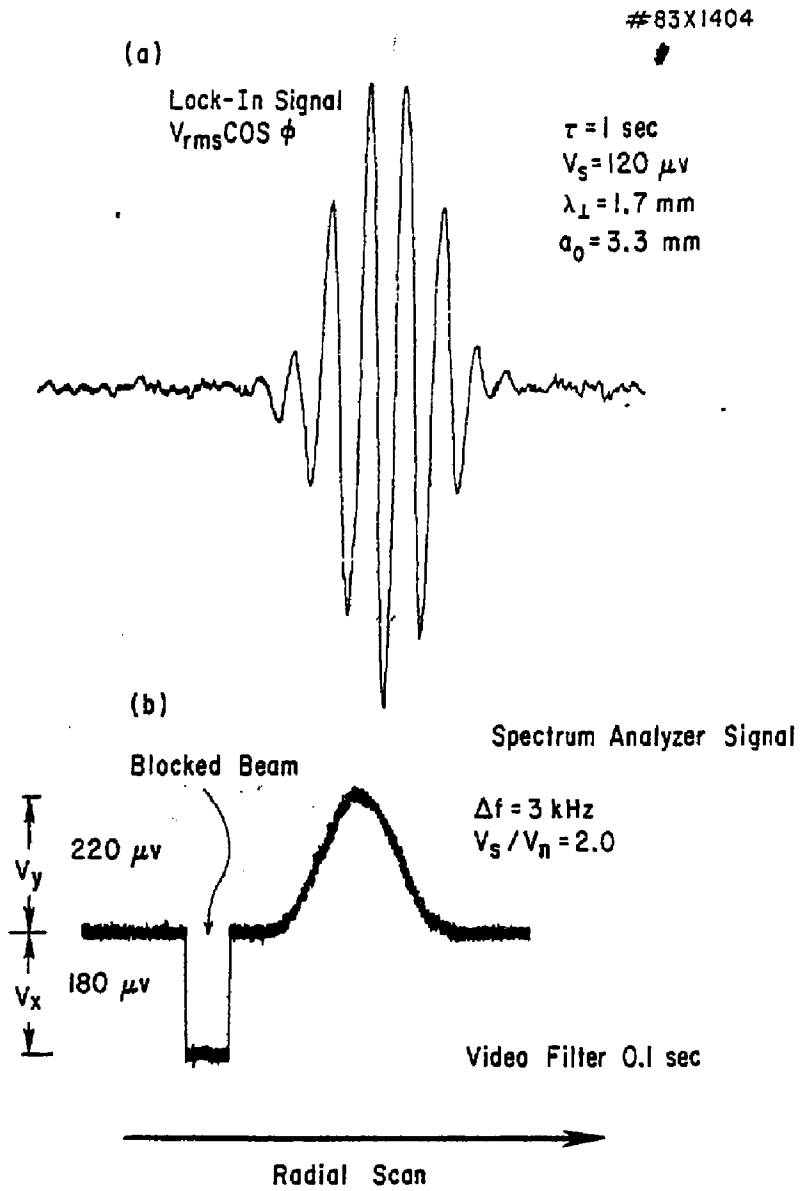
#83X1404
(a)
Lock-In Signal
$V_{rms}COS\ \phi$
$\tau = 1$ sec
$V_s = 120\ \mu v$
$\lambda_\perp = 1.7$ mm
$a_0 = 3.3$ mm
(b)
Spectrum Analyzer Signal
Blocked Beam
$\Delta f = 3$ kHz
$V_s / V_n = 2.0$
V_y
220 μv
V_x
180 μv
Video Filter 0.1 sec
Radial Scan

Fig. 9

#83X1407

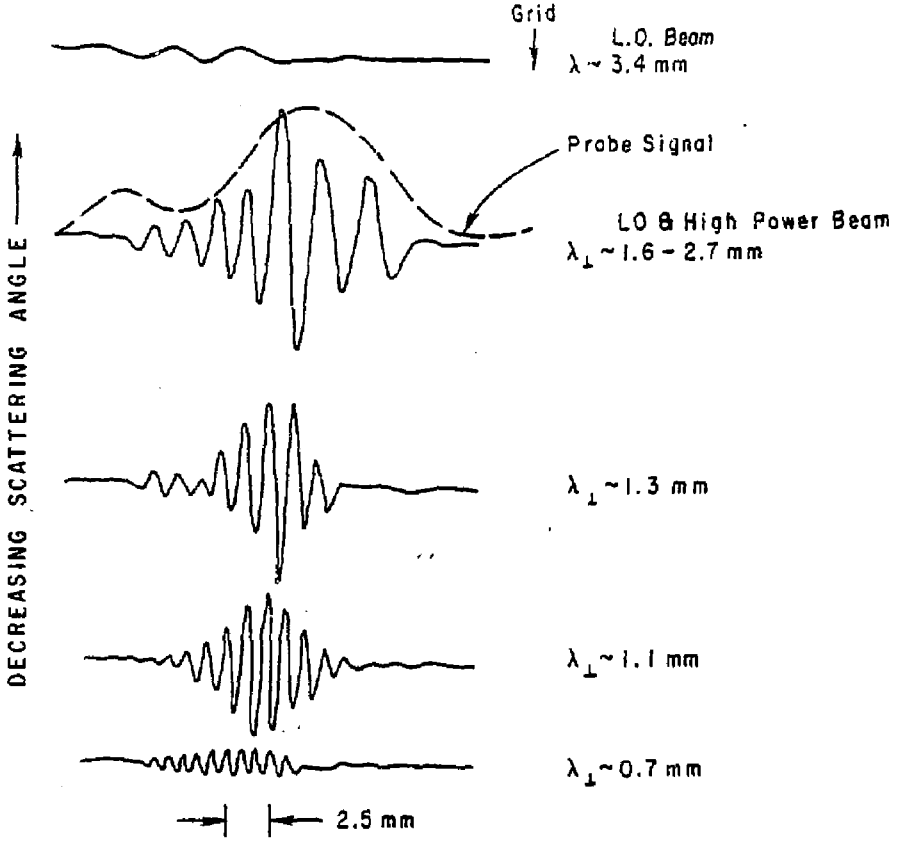

Fig. 10

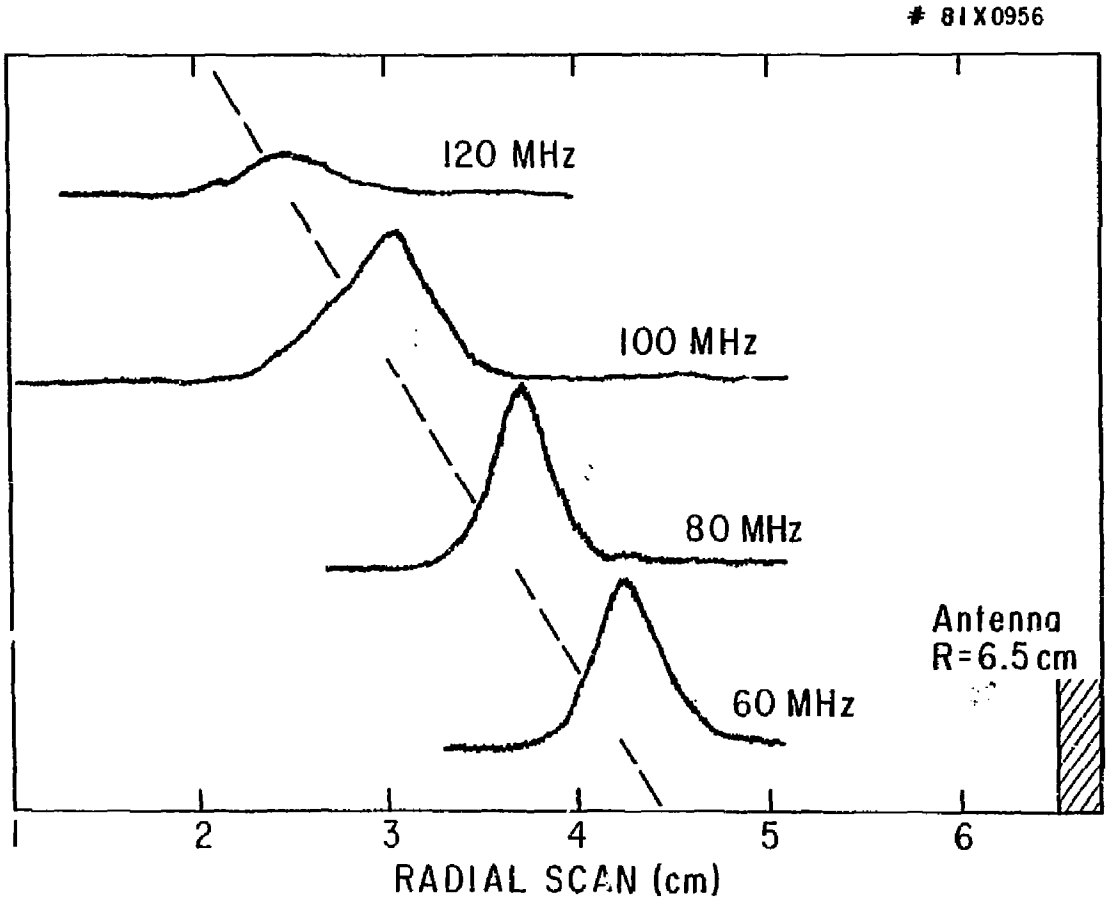
81X0956
120 MHz
100 MHz
80 MHz
60 MHz
Antenna
R=6.5 cm
1
2
3
4
5
6
RADIAL SCAN (cm)

Fig. 11

#83X1411

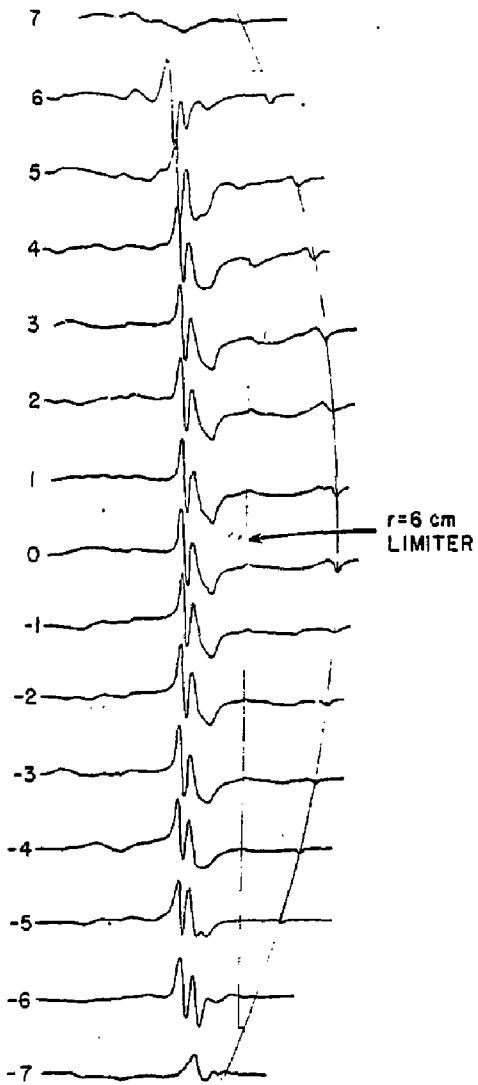

Fig. 12

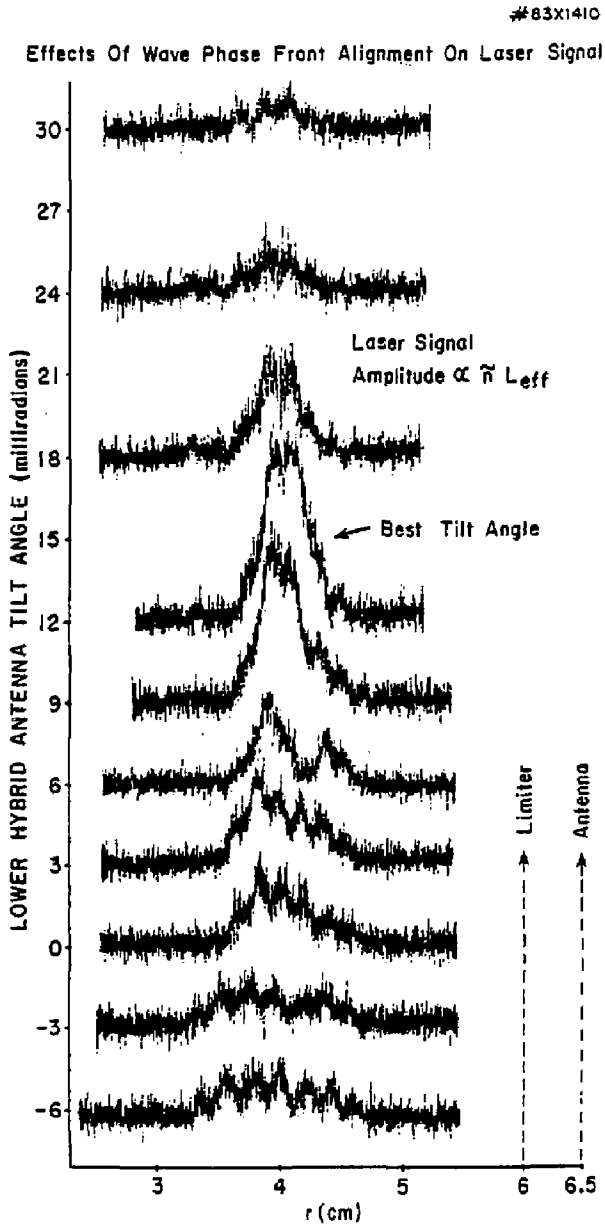
#83X1410
Effects Of Wave Phase Front Alignment On Laser Signal
LOWER HYBRID ANTENNA TILT ANGLE (milliradians)
30
27
24
21
18
15
12
9
6
3
0
-3
-6
Laser Signal
Amplitude ∝ ñ L_eff
Best Tilt Angle
Limiter
Antenna
3
4
5
6
6.5
r (cm)

Fig. 13

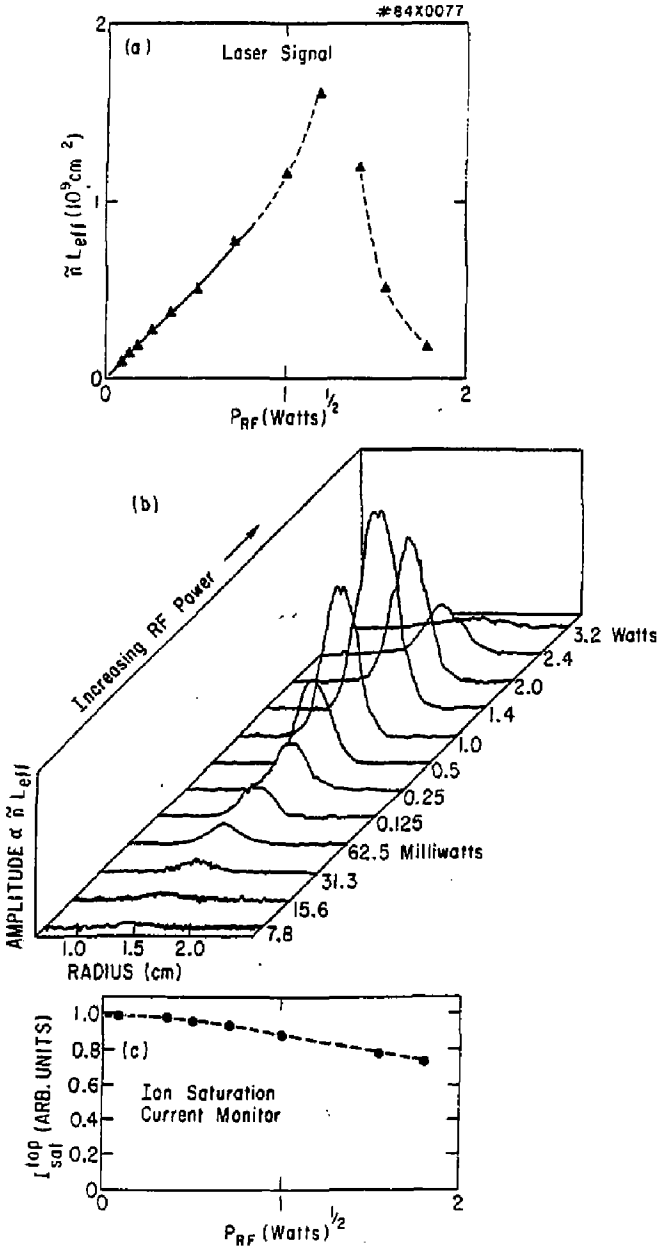
#84X0077
(a)
Laser Signal
$\tilde{n} L_{eff}$ (10^9cm^2)
P_{RF} (Watts)$^{1/2}$
(b)
Increasing RF Power
AMPLITUDE α $\tilde{n} L_{eff}$
3.2 Watts
2.4
2.0
1.4
1.0
0.5
0.25
0.125
62.5 Milliwatts
31.3
15.6
7.8
RADIUS (cm)
(c)
Ion Saturation
Current Monitor
I_{sat}^{top} (ARB. UNITS)
P_{RF} (Watts)$^{1/2}$

Fig. 14

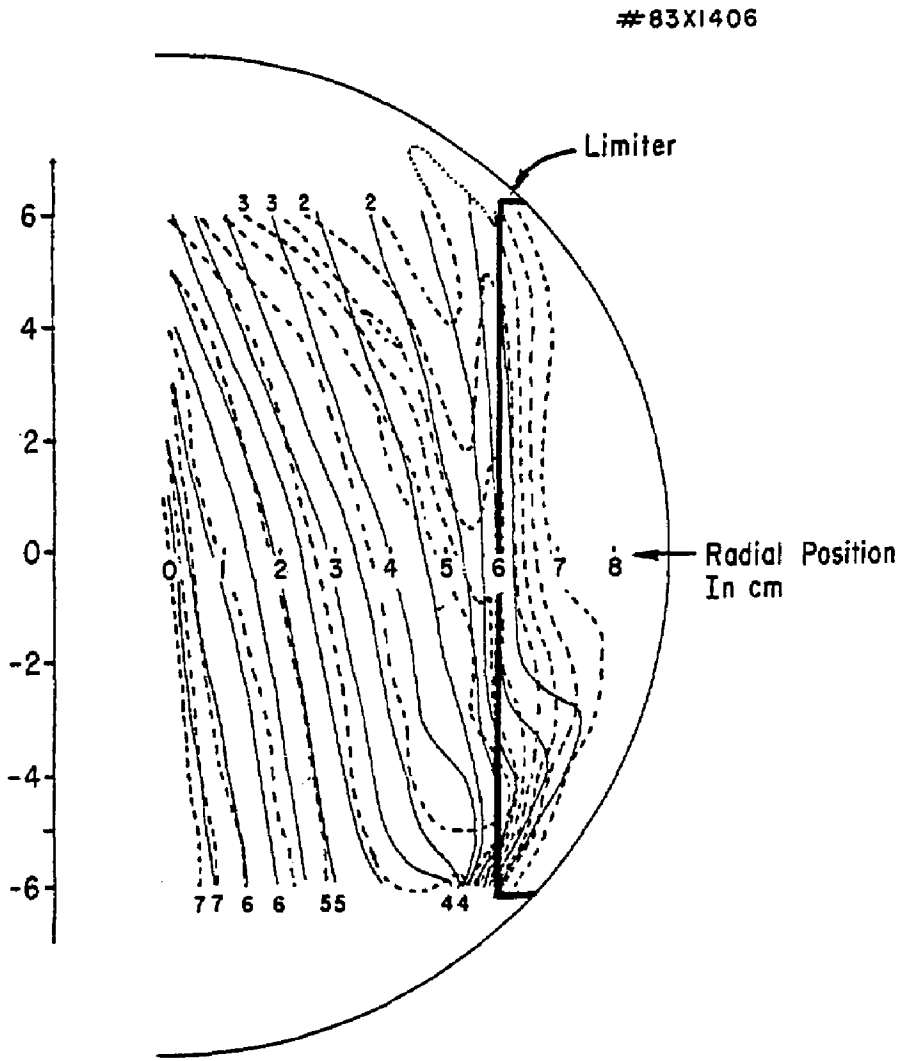
#83X1406
Limiter
6
4
2
0
-2
-4
-6
3 3 2 2
0 1 2 3 4 5 6 7 8
Radial Position
In cm
7 7 6 6 5 5 4 4

Fig. 15

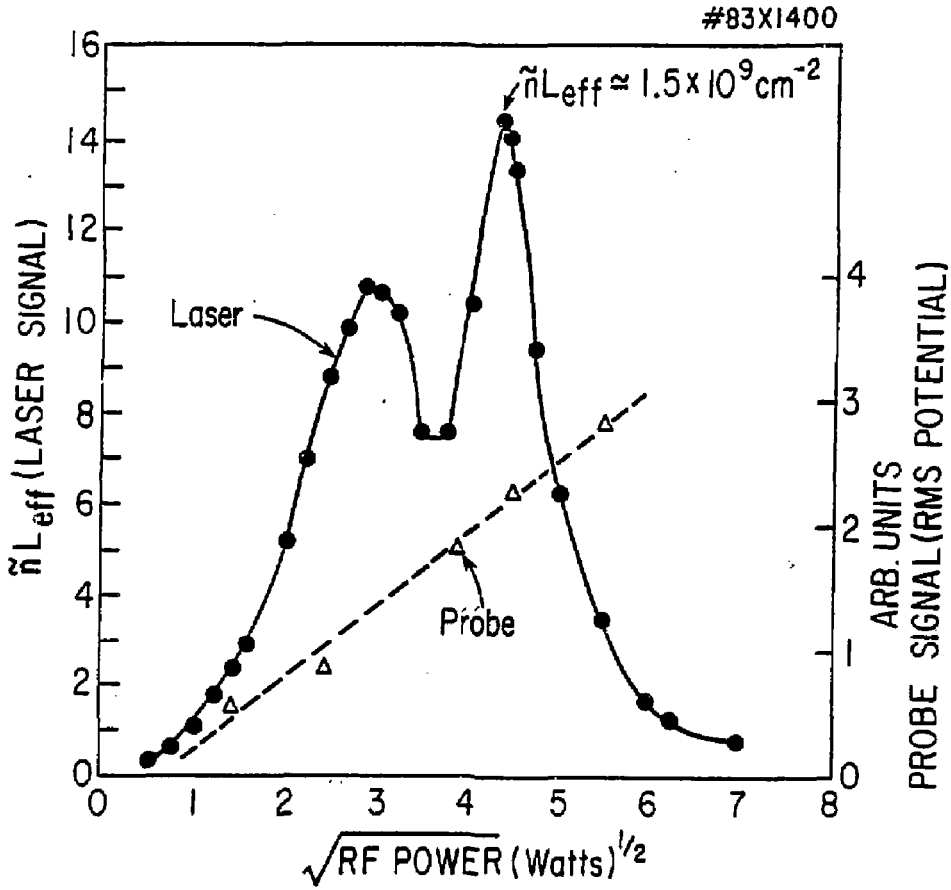
#83X1400
$\tilde{n}L_{eff} \simeq 1.5 \times 10^9 cm^{-2}$
Laser
Probe
$\tilde{n}L_{eff}$ (LASER SIGNAL)
PROBE SIGNAL (RMS POTENTIAL) ARB. UNITS
$\sqrt{RF\ POWER}\ (Watts)^{1/2}$
0
1
2
3
4
5
6
7
8
0
2
4
6
8
10
12
14
16

Fig. 16

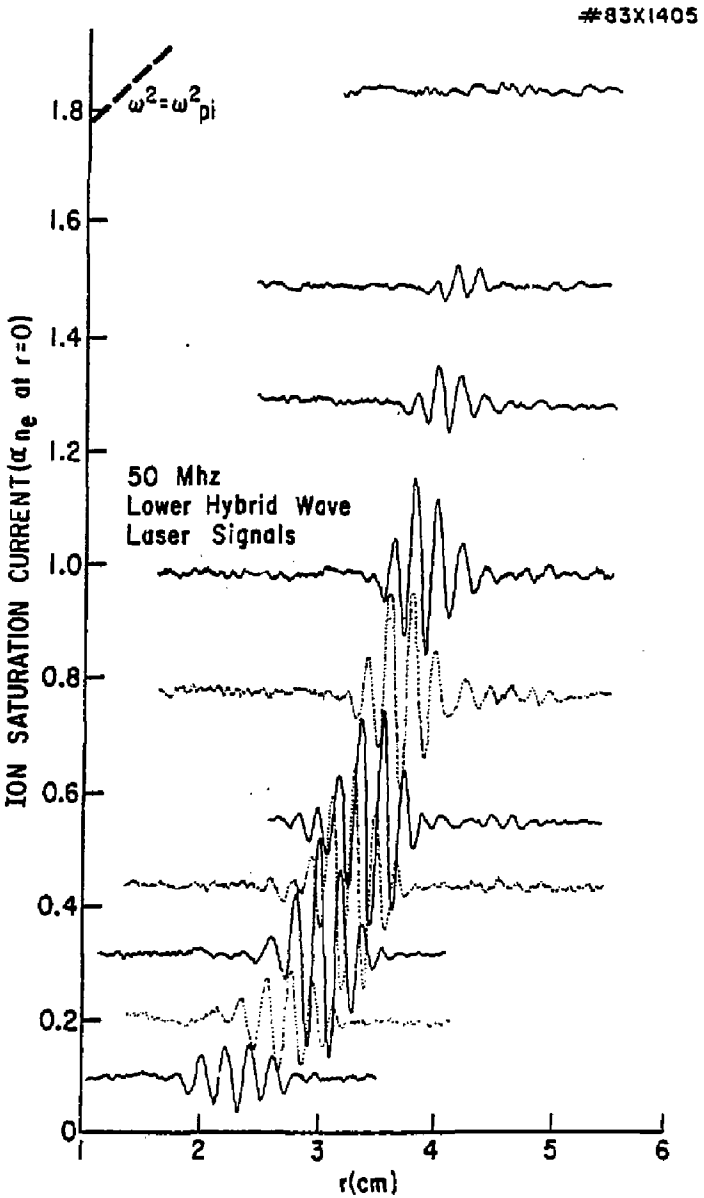
#83X1405
$\omega^2=\omega^2_{pi}$
50 Mhz
Lower Hybrid Wave
Laser Signals
ION SATURATION CURRENT(α n_e at r=0)
1.8
1.6
1.4
1.2
1.0
0.8
0.6
0.4
0.2
0
1
2
3
4
5
6
r(cm)

Fig. 17

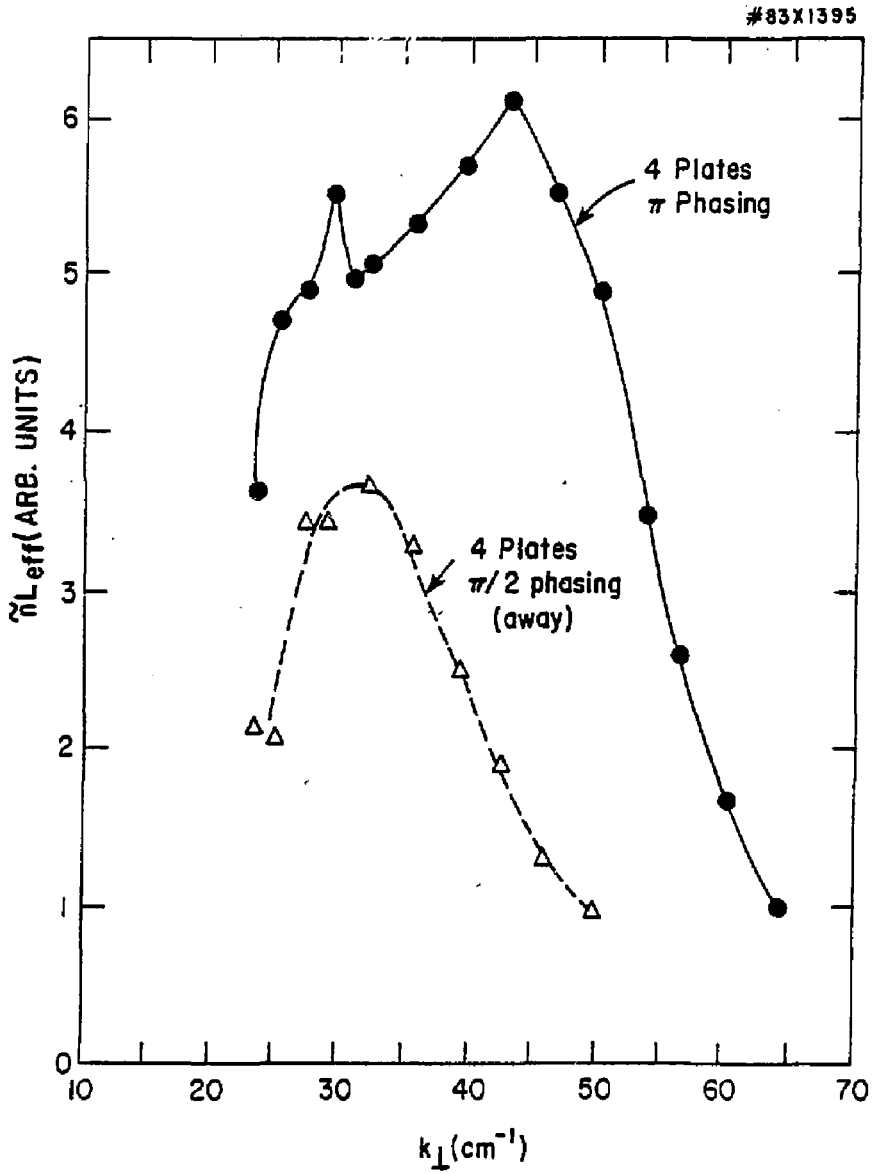
#83X1395
4 Plates
π Phasing
4 Plates
π/2 phasing
(away)
$\tilde{n}L_{eff}$(ARB. UNITS)
$k_\perp(cm^{-1})$
0
1
2
3
4
5
6
10
20
30
40
50
60
70

Fig. 18

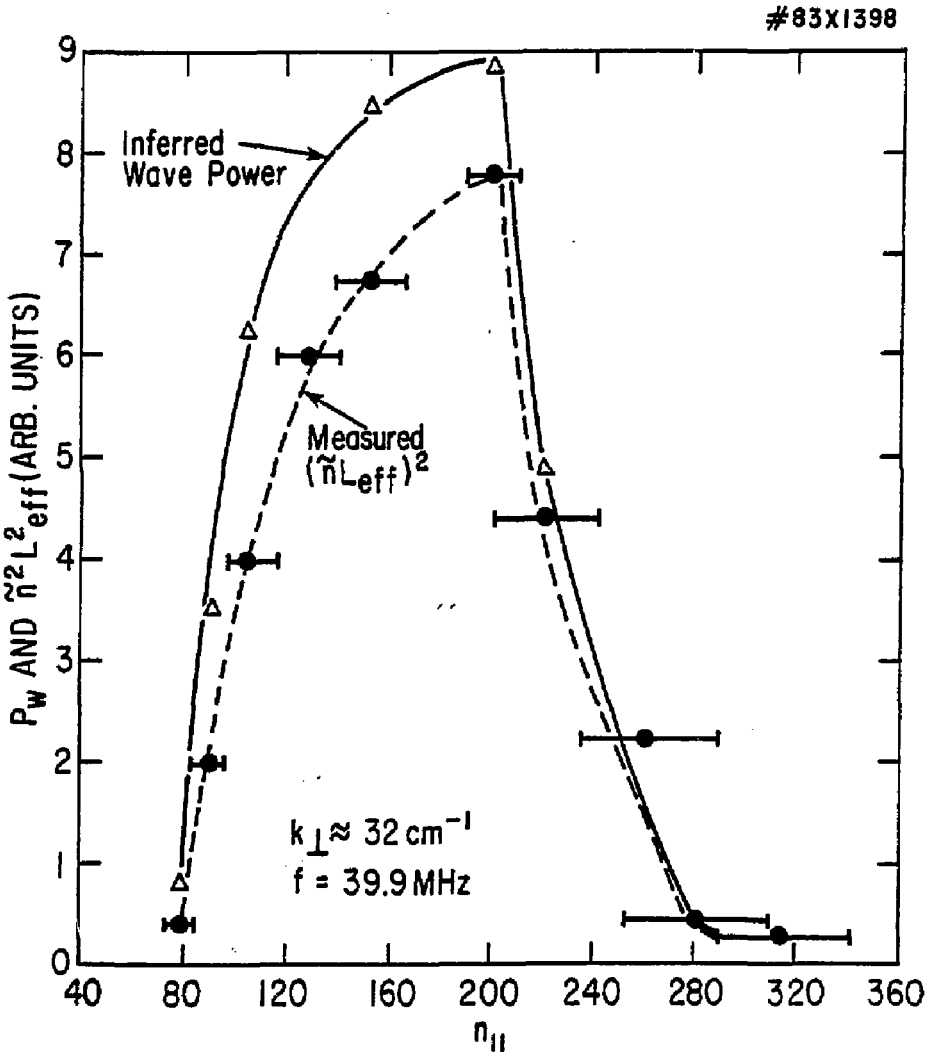
#83X1398
Inferred
Wave Power
Measured
$(\tilde{n}L_{eff})^2$
$k_\perp \approx 32\,cm^{-1}$
f = 39.9 MHz
P_W AND $\tilde{n}^2 L^2_{eff}$ (ARB. UNITS)
$n_{||}$
0
1
2
3
4
5
6
7
8
9
40
80
120
160
200
240
280
320
360

Fig. 19

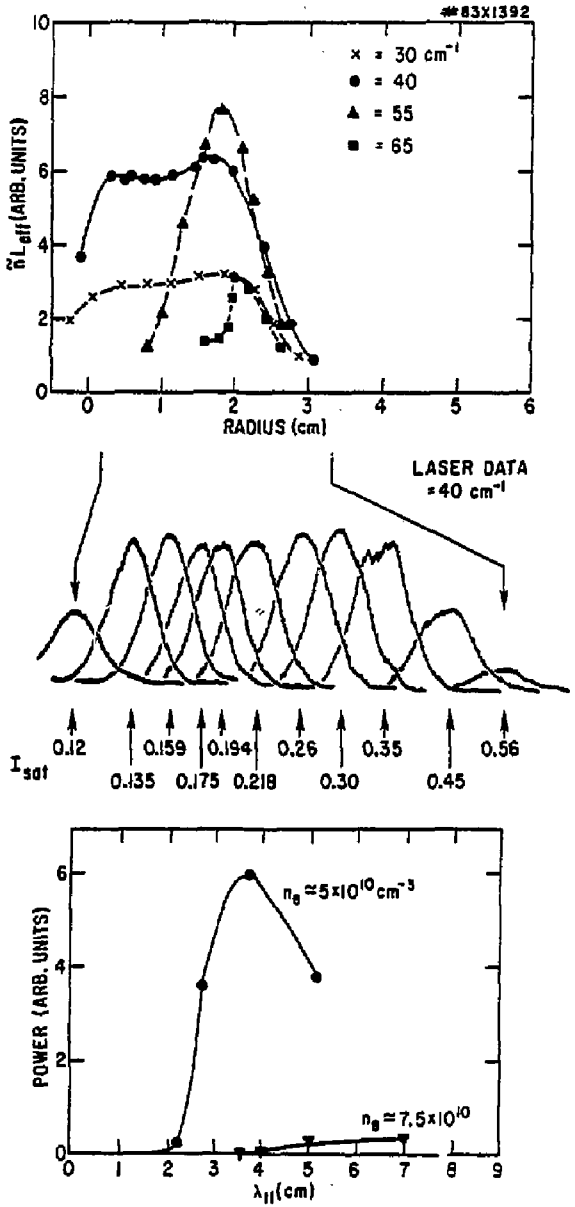
#83X1392
× = 30 cm⁻¹
● = 40
▲ = 55
■ = 65
$\tilde{n}L_{eff}$ (ARB. UNITS)
RADIUS (cm)
LASER DATA
=40 cm⁻¹
I_{sat}
0.12
0.135
0.159
0.175
0.194
0.218
0.26
0.30
0.35
0.45
0.56
POWER (ARB. UNITS)
$n_e \simeq 5\times10^{10}cm^{-3}$
$n_e \simeq 7.5\times10^{10}$
$\lambda_{||}$(cm)

Fig. 20

#84X0076

Frequency Shifted
LHW Laser Signals
Bandwidth $\Delta f = 3$ kHz

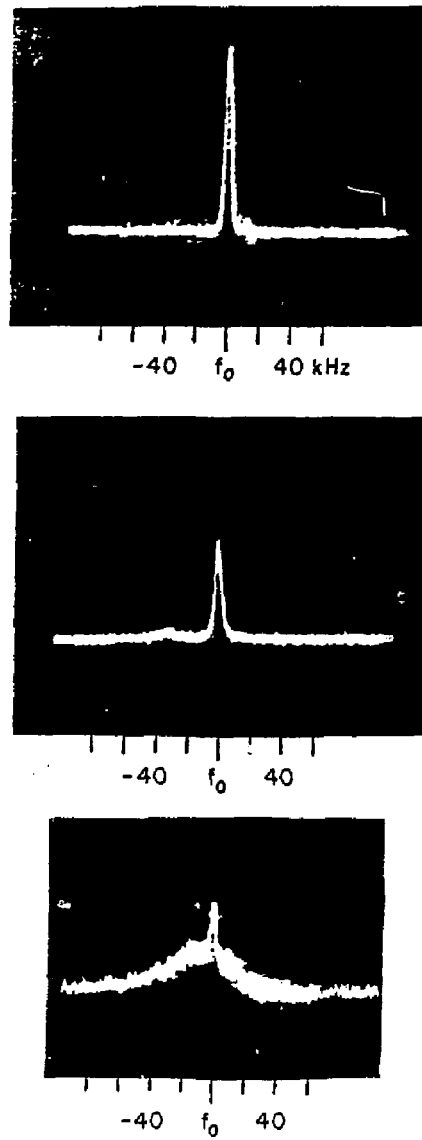

Fig. 21

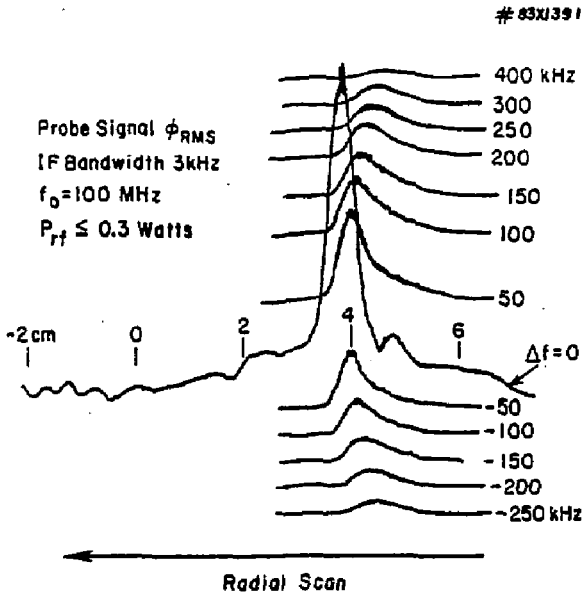
#83X1391
Probe Signal ϕ_{RMS}
IF Bandwidth 3kHz
f_0=100 MHz
$P_{rf} \leq$ 0.3 Watts
400 kHz
300
250
200
150
100
50
-2cm
0
2
4
6
Δf=0
-50
-100
-150
-200
-250 kHz
Radial Scan

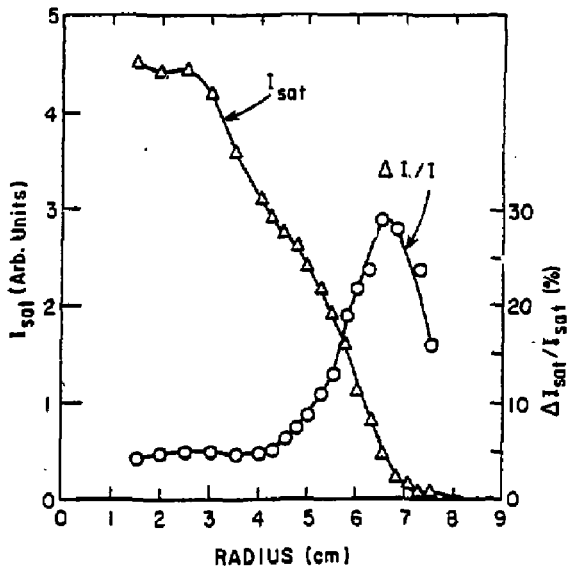
I_{sat}
Δ I/I
I_{sat} (Arb. Units)
$\Delta I_{sat}/I_{sat}$ (%)
RADIUS (cm)
0
1
2
3
4
5
6
7
8
9
10
20
30

Fig. 22

#83X1403

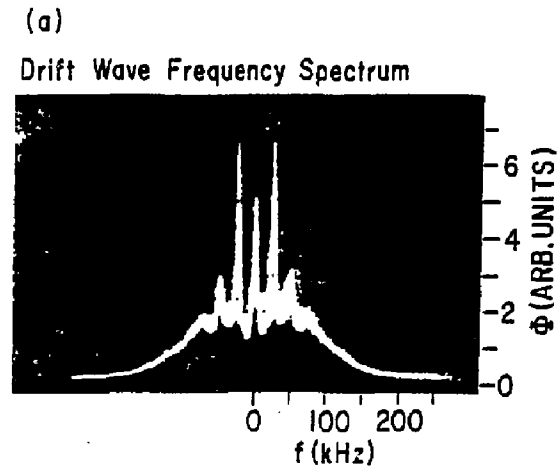

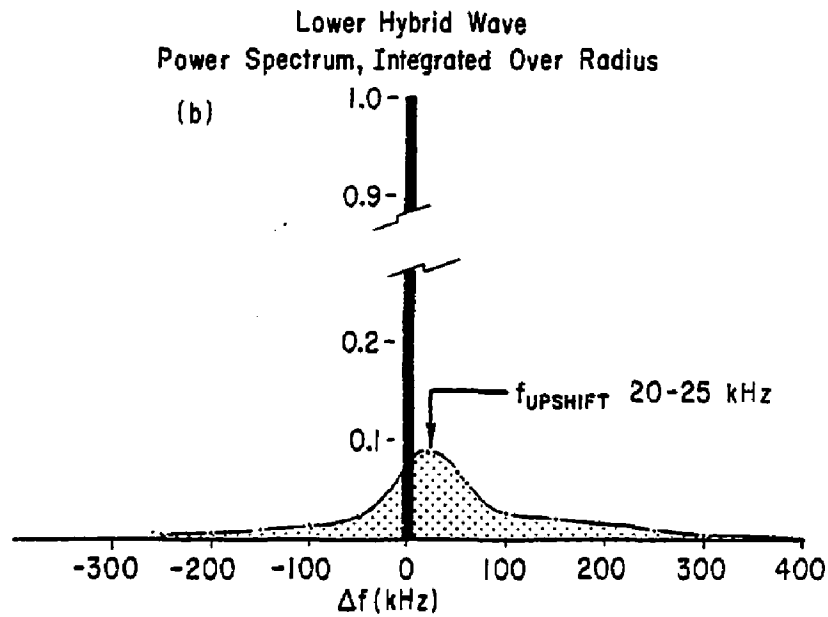

Fig. 23

EXTERNAL DISTRIBUTION IN ADDITION TO TIC UC-20.

Plasma Res Lab, Austra Nat'l Univ, AUSTRALIA
Dr. Frank J. Paoloni, Univ of Wollongong, AUSTRALIA
Prof. I.R. Jones, Flinders Univ., AUSTRALIA
Prof. M.H. Brennan, Univ Sydney, AUSTRALIA
Prof. F. Cap, Inst Theo Phys, AUSTRIA
Prof. Frank Verheest, Inst theoretische, BELGIUM
Dr. D. Palumbo, Dg XII Fusion Prog, BELGIUM
Ecole Royale Militaire, Lab de Phys Plasmas, BELGIUM
Dr. P.H. Sakanaka, Univ Estadual, BRAZIL
Dr. C.R. James, Univ of Alberta, CANADA
Prof. J. Teichmann, Univ of Montreal, CANADA
Dr. H.M. Skarsgard, Univ of Saskatchewan, CANADA
Prof. S.R. Sreenivasan, University of Calgary, CANADA
Prof. Tudor W. Johnston, INRS-Energie, CANADA
Dr. Hannes Barnard, Univ British Columbia, CANADA
Dr. M.P. Bachynski, MPB Technologies, Inc., CANADA
Zhengwu Li, SW Inst Physics, CHINA
Library, Tsing Hua University, CHINA
Librarian, Institute of Physics, CHINA
Inst Plasma Phys, Academia Sinica, CHINA
Dr. Peter Lukac, Komenskeho Univ, CZECHOSLOVAKIA
The Librarian, Culham Laboratory, ENGLAND
Prof. Schatzman, Observatoire de Nice, FRANCE
J. Radet, CEN-BP6, FRANCE
AM Dupas Library, AM Dupas Library, FRANCE
Dr. Tom Mual, Academy Bibliographic, HONG KONG
Preprint Library, Cent Res Inst Phys, HUNGARY
Dr. S.K. Trehan, Panjab University, INDIA
Dr. Indra, Mohan Lal Das, Banaras Hindu Univ, INDIA
Dr. L.K. Chavda, South Gujarat Univ, INDIA
Dr. R.K. Chhajlani, Var Ruchi Marg, INDIA
P. Kaw, Physical Research Lab, INDIA
Dr. Phillip Rosenau, Israel Inst Tech, ISRAEL
Prof. S. Cuperman, Tel Aviv University, ISRAEL
Prof. G. Rostagni, Univ Di Padova, ITALY
Librarian, Int'l Ctr Theo Phys, ITALY
Miss Clelia De Palo, Assoc EURATOM-CNEN, ITALY
Biblioteca, del CNR EURATOM, ITALY
Dr. H. Yamato, Toshiba Res & Dev, JAPAN
Prof. H. Yoshikawa, JAERI, Tokai Res Est, JAPAN
Prof. T. Uchida, University of Tokyo, JAPAN
Research Info Center, Nagoya University, JAPAN
Prof. Kyoji Nishikawa, Univ of Hiroshima, JAPAN
Prof. Sigeru Mori, JAERI, JAPAN
Library, Kyoto University, JAPAN
Prof. Ichiro Kawakami, Nihon Univ, JAPAN
Prof. Satoshi Itoh, Kyushu University, JAPAN
Tech Info Division, Korea Atomic Energy, KOREA
Dr. R. England, Ciudad Universitaria, MEXICO
Bibliotheek, Fom-Inst Voor Plasma, NETHERLANDS
Prof. B.S. Liley, University of Waikato, NEW ZEALAND
Dr. Suresh C. Sharma, Univ of Calabar, NIGERIA
Prof. J.A.C. Cabral, Inst Superior Tech, PORTUGAL
Dr. Octavian Petrus, ALI CUZA University, ROMANIA
Prof. M.A. Hellberg, University of Natal, SO AFRICA
Dr. Johan de Villiers, Atomic Energy Bd, SO AFRICA
Fusion Div. Library, JEN, SPAIN
Prof. Hans Wilhelmson, Chalmers Univ Tech, SWEDEN
Dr. Lennart Stenflo, University of UMEA, SWEDEN
Library, Royal Inst Tech, SWEDEN
Dr. Erik T. Karlson, Uppsala Universitet, SWEDEN
Centre de Recherchesen, Ecole Polytech Fed, SWITZERLAN
Dr. W.L. Weise, Nat'l Bur Stand, USA
Dr. W.M. Stacey, Georg Inst Tech, USA
Dr. S.T. Wu, Univ Alabama, USA
Prof. Norman L. Oleson, Univ S Florida, USA
Dr. Benjamin Ma, Iowa State Univ, USA
Prof. Magne Kristiansen, Texas Tech Univ, USA
Dr. Raymond Askew, Auburn Univ, USA
Dr. V.T. Tolok, Kharkov Phys Tech Ins, USSR
Dr. D.D. Ryutov, Siberian Acad Sci, USSR
Dr. G.A. Eliseev, Kurchatov Institute, USSR
Dr. V.A. Glukhikh, Inst Electro-Physical, USSR
Institute Gen. Physics, USSR
Prof. T.J. Boyd, Univ College N Wales, WALES
Dr. K. Schindler, Ruhr Universitat, W. GERMANY
Nuclear Res Estab, Julich Ltd, W. GERMANY
Librarian, Max-Planck Institut, W. GERMANY
Dr. H.J. Kaeppler, University Stuttgart, W. GERMANY
Bibliothek, Inst Plasmaforschung, W. GERMANY